Lee, M. (2010) *Transmission electron microscopy (TEM) of earth and planetary materials: a review.* Mineralogical Magazine, 74 (1). pp. 1-27. ISSN 0026-461X

http://eprints.gla.ac.uk/25484/

Deposited on: 23 March 2010

Enlighten – Research publications by members of the University of Glasgow
http://eprints.gla.ac.uk

Transmission electron microscopy (TEM) of Earth and planetary materials: A review

M. R. LEE
Department of Geographical and Earth Sciences, University of Glasgow, Gregory Building, Glasgow G12 8QQ, U.K.

E-mail: Martin.Lee@ges.gla.ac.uk

Abstract

Using high intensity beams of fast electrons the transmission electron microscope (TEM) and scanning transmission electron microscope (STEM) enable comprehensive characterization of rocks and minerals at micrometre to sub-nanometre length scales. This review outlines the ways in which samples of Earth and planetary materials can be rendered sufficiently thin for TEM and STEM work, and highlights the significant advances in site-specific preparation enabled by the focused ion beam (FIB) technique. Descriptions of the various modes of TEM and STEM imaging, electron diffraction and X-ray and electron spectroscopy are outlined, with an emphasis on new technologies that are of particular relevance to geoscientists. These include atomic resolution Z-contrast imaging by high angle annular dark-field STEM, electron crystallography by precession electron diffraction, spectrum mapping using X-rays and electrons, chemical imaging by energy-filtered TEM and true atomic resolution imaging with the new generation of aberration corrected microscopes. Despite the sophistication of modern instruments, the spatial resolution of imaging, diffraction and X-ray and electron spectroscopy work on many natural materials is likely to remain limited by structural and chemical damage to the thin samples during TEM and STEM.

26 **Introduction**
27 Conventional transmission electron microscopy (TEM), and the closely related technique of
28 scanning transmission electron microscopy (STEM), can provide microstructural, crystallographic,
29 compositional and electronic information from micrometre to sub-nanometre sized regions of thin
30 samples. Despite the power of these techniques, they have the reputation within geoscience of
31 requiring difficult and time consuming sample preparation and of yielding images, diffraction
32 patterns and analytical data that can be interpreted only with extensive knowledge of electron-
33 beam specimen interactions. However, recent improvements in technologies for preparing thin
34 samples of rocks and minerals, coupled with computerization and automation of microscope
35 functions including digital capture and processing of results, has made the technique much more
36 accessible. Here are described the processes of TEM and STEM work, from sample preparation to
37 the various modes of imaging, electron diffraction, and X-ray and electron spectroscopy, hopefully
38 in a manner that is accessible to the non-expert geoscientist. For a comprehensive theoretical and
39 practical account of the interaction of electrons with thin specimens see Loretto (1994) and
40 Williams and Carter (1996). Descriptions of TEM and related techniques with a geoscience
41 emphasis can also be found in McLaren (1991) and Buseck (1992), and Putnis (1992) provides a
42 very accessible account of the use of TEM imaging and electron diffraction in mineralogy.
43 Hereafter '(S)TEM' denotes both the conventional TEM and STEM techniques whereas TEM and
44 STEM are referred to individually where differences between the two techniques are important.
45 TEM became an important geoscience tool in the 1970s, when ion beam milling enabled the
46 preparation of high quality thin samples of rocks and minerals. This provided the impetus for
47 research into those processes whose products were observable at micrometre to sub-micrometre
48 scales, for example exsolution in feldspars and pyroxenes (see review by Champness 1977). The
49 last thirty years have witnessed dramatic advances in microscope technologies, leading to the
50 widespread availability of techniques such as STEM high angle annular dark-field (HAADF)
51 imaging, chemical imaging by energy filtered TEM (EFTEM) and spectrum mapping using
52 energy-dispersive X-ray analysis (EDX) and electron energy loss spectroscopy (EELS). One of the
53 most significant recent advances has been in lens design, culminating in the development of
54 microscopes with aberration corrected optics that can achieve sub-Ångstrom (i.e. <0.1 nm) point-
55 to-point resolutions (O'Keefe, 2008; Muller, 2009). Atomic scale imaging is crucial for the
56 characterization of advanced functional materials such as superconductors and transistors (Muller,
57 2009; Urban, 2009), and so is also central to the burgeoning field of nanotechnology.
58 Owing to the fine-scale heterogeneity of many Earth and planetary materials, the ability to
59 comprehensively characterize them at the nanoscale is actually a double-edged sword, and the
60 geoscientist must take great care to relate results from (S)TEM back to the bulk sample (Hochella
61 *et al.*, 1999). This point is emphasized by Williams and Carter (1996), who estimated that in the
62 time between instruments first becoming commercially available (in the 1950s) and their time of
63 writing, only 0.6 mm^3 of material had been studied by TEM. The present review has therefore
64 been prompted by the development over the last decade of two technologies that greatly enhance
65 the representativeness and relevance of (S)TEM work for geoscientists. The first is the focused ion

66 beam (FIB) technique, which is used to prepare the very thin samples required for (S)TEM from
67 specific sites on the surface of samples ranging from rough grains to polished thin sections. FIB
68 technology has revitalized interest in (S)TEM amongst geoscientists as the two techniques in
69 combination represent a 'microstructural microprobe'. This is because they enable comprehensive
70 characterization of thin samples that can be extracted from the bulk material with the same spatial
71 accuracy (i.e. better than a few micrometres) as analyses by techniques including electron probe
72 microanalysis (EMPA) and secondary ion mass spectrometry. The second technical development
73 is electron backscatter diffraction (EBSD), which is a SEM based method whereby electron
74 backscatter (Kikuchi) patterns are obtained from polished samples of rocks and minerals for
75 quantitative characterization of their microtextures (Prior *et al.* 1999). The dramatic increase over
76 the last decade in rates of Kikuchi pattern acquisition, and the development of sophisticated
77 software for pattern indexing and data presentation, has stimulated microstructural research in
78 areas ranging from structural geology to biomineralization. Whilst not directly related to (S)TEM,
79 this increasing volume of research has drawn new attention to the wealth of information on
80 crystallization, alteration and deformation that can be obtained from the microstructures and
81 microtextures of rocks and minerals. In fact, EBSD has supplanted (S)TEM in some applications,
82 such as visualizing deformation within single crystals (Reddy *et al.,* 2006), mapping the textures
83 of polycrystalline samples over tens of micrometre scales (e.g. Watt *et al.,* 2006), and facilitating
84 the non-destructive identification of new minerals (Mikouchi *et al.,* 2009), but the two techniques
85 are particularly powerful when used together (e.g. Lee and Ellen, 2008).
86
87 **Which method of sample preparation?**
88 One of the principal hurdles to the more widespread use of (S)TEM by geoscientists has been
89 sample preparation. The challenge is to render the sample sufficiently thin so that when irradiated
90 with a ~100-300 kV electron beam the incident electrons can pass through the sample and without
91 being scattered too highly or losing a significant proportion of their initial energy. A suitably thin
92 sample is often termed 'electron transparent'. The target thickness is dependent on the material
93 and the application. For general TEM imaging and electron diffraction work on silicate minerals
94 ~100 nm is acceptable, but for analysis by EELS the samples should contain areas that are thinner
95 (<~50 nm), and atomic resolution TEM imaging requires regions that are ≤~10 nm thick and free
96 of damage to their crystal structure. As lenses are not used to form STEM images, the thickness
97 requirements for STEM samples are typically less stringent than for TEM. Below are described the
98 four main ways in which electron-transparent samples can be prepared from Earth and planetary
99 materials.
100
101 *Mechanical and chemical comminution*
102 The main method for producing electron transparent samples of insulators prior to the
103 development of ion milling in the 1970s (e.g. Barber 1970) was grinding them to a powder.
104 Typically the sample is crushed, or a specific region abraded using a drill, and the powder
105 deposited on a carbon film (Fig. 1*a*); some of the constituent grains will have sufficient electron

106 transparent area for study. Mechanical preparation is still used where ion beam techniques are
107 inappropriate owing to their potential for structural damage and compositional modification, for
108 example in the characterization of amorphous layers on chemically ‘leached’ mineral surfaces (e.g.
109 Casey *et al.,* 1989; Zhu *et al.,* 2006) and high precision EELS work (e.g. Garvie and Buseck,
110 1999). If the sample already comprises sub-micrometre sized grains, they can be deposited onto a
111 carbon film for study and without further preparation (Fig. 1*a*). This method has been used to
112 study samples including airborne particulates (e.g. Leppard 2008) and groundwater colloids
113 (Utsunomiya *et al.,* 2009), and is also ideal for the characterization of the constituents of acid-
114 resistant residues of rocks (e.g. Lee *et al.*, 1995) (Fig. 1*a, b*) and minerals (e.g. Ma *et al.,* 2002).
115
116 *Ultramicrotome*
117 This is the preferred technique for preparation of biological samples, which are typically
118 embedded in a resin block and thin slices are serially cut from its surface using a glass or diamond
119 knife. Ultramicrotome is usually unsuitable for brittle rock and minerals as it generates fractures
120 and defects, but has been used to make electron transparent samples of grains enclosed by fungal
121 and algal cells within lichens (Barker and Banfield, 1996), acid mine drainage sediments
122 (Hochella *et al.,* 1999) and interplanetary dust particles (e.g. Bradley and Brownlee, 1986; Stephan
123 *et al.,* 1994). A particularly successful recent application has been to prepare thin samples of sub-
124 micrometre sized cometary particles that were captured within aerogel, a very low density silica
125 glass, during the NASA Stardust mission (Fig. 2) (e.g. Leroux *et al.* 2008; Zolensky *et al.* 2008).
126
127 *Ion milling*
128 Ion milling is used extensively to prepare thin samples (hereafter ‘foils’) of rocks and minerals.
129 Geoscientists typically prepare the foils from thin sections mounted in a resin that dissolves in
130 acetone or Lakeside (Barber, 1981). Following extraction from the thin section the sample is
131 loaded in the ion mill and bombarded at low angles from above and below, typically with a ≤5 kV
132 Ar^+ ion beam but sometimes with neutral atoms, so that it gradually thins by sputtering. It is
133 difficult to mill the foil to a uniform thickness owing to the generation of topography and
134 differential sputtering rates if the sample is coarsely polymineralic. Milling usually proceeds until
135 the sample has been perforated and electron transparent areas are available around the holes. Ion
136 milling is very effective for most silicates and carbonates, but all materials experience some
137 damage and it can be severe for minerals such as halite and sylvite (Barber, 1993). The impact of
138 an ion or atom will deposit ~5 keV of energy into $\sim10^{-25}$ m^{-3} of the sample, which will be
139 accompanied by a cascade of displaced atoms and a local increase in temperature (≥ ~100°C of
140 heating, which is greatest on the outermost part of the foil; Barber, 1993). This damage will
141 produce a thin amorphous and ion-implanted layer on all milled surfaces, which may be
142 susceptible to oxidation. For any one material, the depth of ion implantation and associated
143 damage will vary with accelerating voltage and milling angle; for example calculations using
144 SRIM software (Ziegler 2003) show that 5 kV Ar^+ argon ions will be implanted up to 10 nm into
145 quartz, even if milling at a very shallow angle of 1.5°. Diffuse scattering of electrons by damage

146 layers will degrade high-resolution TEM images and electron diffraction patterns, and the presence
147 of oxygen and implanted argon will complicate the interpretation of chemical analyses by EDX
148 and EELS (Barber, 1993), and EELS valence determinations (Heard *et al.*, 2001; Garvie *et al.,*
149 2004).
150
151 *Focused Ion Beam (FIB) technique*
152 The FIB technique uses high energy heavy ions, typically 30 kV Ga^+, to cut pairs of trenches into
153 the surface of a sample to leave thin relict walls that then can be cut free and mounted as a
154 (S)TEM foil (Fig. 3*a*). In the last decade this technique has been used extensively by geoscientists
155 to prepare foils of terrestrial rocks and minerals (e.g. Heaney *et al.,* 2001; Wirth, 2004, 2009; Lee
156 *et al.*, 2007) and extraterrestrial samples (Stroud *et al.,* 2000; Lee *et al.,* 2003; Zega *et al.,* 2007;
157 Chizmadia *et al.,* 2008). Foils may be prepared from polished thin sections, or from the surfaces of
158 grains extracted from their rock matrices (e.g. Zega *et al.,* 2007) or collected from soils (e.g. M.R.
159 Lee *et al.,* 2007, 2008*a*, *b*) (Fig. 3*a–b*).
160 The use of the FIB technique in geoscience has been recently reviewed in detail by Wirth
161 (2009) and so is only summarized below. Currently two varieties of FIB instrument are in use. The
162 older 'single beam' models use ions for both imaging and milling, with the obvious drawback that
163 the bulk sample and foil will be damaged by ion implantation during imaging. The newer 'dual
164 beam' instruments have an electron gun so that the foil can be imaged at high resolutions and with
165 minimal damage before, during and after ion milling. Foil manufacture using both models is
166 similar, although final sample extraction usually differs. Insulators are coated with carbon or gold
167 prior to FIB work then a protective strap, typically platinum, is deposited over the area of interest
168 by interaction of an injected organometallic gas with the ion/electron beam. Ion beam deposition is
169 considerably quicker, but during the early stages of deposition Ga^+ ions may be implanted into the
170 sample to a depth of tens of nanometres rendering it amorphous. This problem and ways to
171 mitigate it has been discussed by Lee *et al.* (2007). In the next stage a pair of ~15-20 µm long by
172 ~10 µm wide and ~7 µm deep trenches are milled astride the area of interest. The ~1000 nm thick
173 sample remaining is then 'polished' using the ion beam oriented at a glancing angle (~1.5°) to its
174 vertical sidewalls until it attains ~100 nm thickness (Fig. 3*a*). At this stage the foil is cut away at
175 its edges and base (Fig. 3*b*), lifted out using an *ex-situ* micromanipulator and placed on a carbon
176 film for study (Fig. 3*c*). Supporting the foil on a holey carbon film can be problematic as the edges
177 of the holes may be visible in some images, and unless the area of interest lies over a hole the
178 carbon will complicate interpretation of EDX and EELS analyses (Zega *et al.,* 2007).
179 Using a dual-beam instrument the foil may be lifted out with an *in-situ* micromanipulator
180 when still ~1000 nm thick, then welded to the tines of a holder using ion and/or electron beam
181 deposited platinum (Fig. 3*d*); an alternative method described by Zega *et al.* (2007) is to support
182 the foil using a set of microtweezers manufactured using the ion beam. Subsequently the foil is
183 milled to electron transparency and then removed from the FIB for further study. Dual-beam
184 instruments give much better control over the milling process, and as the foil is lifted out *in-situ*
185 and at ~1000 mm thickness there is much less chance of breakage. This method of mounting the

foil also removes any potential deleterious effects of a supporting carbon film on images and analyses. Additionally, all of those techniques traditionally associated with SEM (e.g. EDX and EBSD) can be used on a dual-beam FIB with the further advantage that 3D reconstruction of the sample can be undertaken by serial cutting and imaging (Wirth, 2009).

The major advantage of FIB over other preparation methods is that the foils may be cut from within <1 μm of the desired site on the sample surface, very little material is destroyed in the process (~2300 μm^3; Wirth, 2009), there is minimal differential milling of polycrystalline samples and the foils can be cut to a uniform thickness. The FIB has found applications including the preparation of foils from sub-micrometre sized inclusions within rock matrices (Chizmadia *et al.*, 2008; Lee and Ellen, 2008) and from the interfaces between different generations of minerals (Seydoux-Guillaume *et al.,* 2003; Zega *et al.*, 2007; Hay *et al.*, 2009). As the FIB enables cross-sectioning of the outermost few micrometres of rough grains, it can also be used to study coatings of weathering products (e.g. Lee *et al.*, 2008*b*) (Fig. 3*b*) and microbes (Obst *et al.,* 2005; Benzerara *et al.,* 2005; Lee *et al.,* 2008a; Bonneville *et al.,* 2009) (Fig. 3*a*), and together with surface-sensitive analysis techniques such as X-ray photoelectron spectroscopy to characterize chemical modification to weathered grain surfaces (Lee *et al.,* 2008a). In common with Ar^+ ion milling, amorphous envelopes form on all Ga^+ ion milled surfaces. For an angle of incidence of 90°, 30 kV Ga^+ ions will be implanted into quartz to a depth of ~50 nm and to a depth of ~20 nm even when 'polishing' at a glancing angle of 1.5° (calculated using SRIM software; Ziegler 2003). The amorphous envelopes may be thinned significantly by final polishing using lower energy (e.g. 5 kV) Ga^+ ions, which will be implanted to <~10 nm, or the foil can be polished *ex-situ* using a low energy (<1 kV) Ar^+ ion mill. The presence of amorphous envelopes on foil surfaces is nonetheless a particular problem if attempting to make <~50 nm thick foils for high-resolution TEM imaging or EELS work.

Sample preparation summary

Argon ion milling remains the best technique for making foils with substantial electron transparent areas and with regions sufficiently thin (<few 10s nm) for high-resolution imaging and high spatial resolution EDX and EELS spot analyses. Damage can be minimized by using appropriate accelerating voltages and milling angles, but if thin samples completely free of milling artifacts are required, then mechanical comminution or ultramicrotome are the best methods. The principal advantages of FIB over argon ion milling are its ability to: (i) cut foils from essentially anything that can be physically accommodated by the instrument and remain stable at high vacuum and under ion bombardment, (ii) extract thin samples from within <1 μm of the desired site, (iii) rapidly prepare thin samples of a very wide range of materials, from loose aggregates of clays to diamonds (Heaney *et al.*, 2001) and (iv) produce foils of constant thickness (i.e. parallel sided), which are ideal for EDX and EELS mapping.

TEM and STEM instruments

For (S)TEM work the washer or grid that supports the loose grains, ultramicrotome slices or ion milled foils, is secured in a rod holder, part of which is then inserted, *via* an airlock, into the electron column. The sample is illuminated using a ~100-300 kV electron beam generated from a thermionic source (W or LaB_6) or field-emission gun (FEG). TEM imaging and electron diffraction uses an electron beam that is broad (several micrometres) and for most purposes parallel. Lenses beneath the sample form the image or diffraction pattern that is viewed directly on a fluorescent screen or, more commonly now electronically *via* a camera located above or below the screen (Fig. 4). Many modern TEMs can also be operated in STEM mode, whereby the electron beam is converged to a very small probe (sub-nanometre sized for FEG instruments) that can be rastered over the thin sample and images are formed using electron detectors (Fig. 4). The instrument's post-sample optics are not used in STEM mode and they are absent altogether from dedicated STEM instruments. Until recently geoscientists mainly used TEM, but STEM is now finding many applications, particularly for high spatial resolution atomic number (Z) contrast imaging, nanoscale electron diffraction, and EDX and EELS work. For imaging, STEM has the advantage over conventional TEM of delivering a lower electron dose (as the probe is rapidly scanned over the sample), thus facilitating the study of beam sensitive materials. STEM is also better than TEM for studying thick (i.e. hundreds of nanometre to few micrometres) samples as its image formation is relatively unaffected by chromatic or spherical aberration.

(S)TEM imaging and electron diffraction utilise the (predominantly) elastic forward scattering of incident electrons by atomic nuclei in the thin sample (Fig. 5). The scattered electrons change direction (mainly by <~3°) but lose very little energy; those electrons that pass close to the nucleus can however be scattered at higher angles (up to 180°, i.e. backscattering) and lose some energy (i.e. scattering is not truly elastic). The two mechanisms by which contrast is generated in (S)TEM images (amplitude and phase contrast) are described below, and examples are given of the different ways in which this contrast can be utilized in geoscience research.

(S)TEM amplitude contrast imaging

Amplitude contrast is the product of variations in the intensity or angle of electron scattering throughout the volume of the thin sample illuminated by the incident beam. These images are formed by isolating (or 'filtering') electrons that have been scattered over a certain angular range in one of two ways, termed 'bright-field' and 'dark-field'. Bright-field uses the 'direct beam', which contains unscattered and low angle forward scattered electrons (Fig. 5). In TEM mode these electrons are isolated with the objective aperture whereas in STEM mode an electron detector lying on the optic axis is used (Fig. 6). Dark-field images are formed solely from forward scattered electrons. In TEM mode the incident beam is tilted so that scattered electrons are accepted by the objective aperture (for crystalline materials typically a single Bragg scattered beam), whereas STEM dark-field imaging uses annular (ring-shaped) detectors. These detectors intercept all those electrons that have been scattered over a certain angular range; collection semi-angles of >~0.5 to 3° yield annular dark-field (ADF) images (also termed 'low angle annular dark-field', or LAADF)

266 whereas semi-angles of ~3 to 10° provide high angle annular dark-field (HAADF) images (Fig. 6).
267 The distinction between LAADF and HAADF may be made by using separate detectors (Fig. 6),
268 or by changing the diffraction camera length (effectively the magnification of the diffraction
269 pattern) so that different angular ranges can be captured using a single fixed annular detector.
270 Three properties of a thin sample will determine the intensity and angle of scattering of the
271 incident beam and so its appearance in bright- and dark-field images: thickness (*t*) and atomic
272 mass (Z) (together termed mass-thickness contrast), and Bragg diffraction (only in crystalline
273 materials). The ways in which these properties produce contrast that is useful to the geoscientist
274 are described below.
275
276 *Mass-thickness contrast*
277 Mass-thickness contrast is an outcome of incoherent elastic scattering of incident electrons by the
278 thin sample, the intensity of which increases with both Z and *t*. Thus, thicker and higher Z regions
279 of a sample will be relatively dark in bright-field images because a high proportion of incident
280 electrons are being scattered, thus lowering the intensity of the direct beam. Thickness contrast is
281 most important at scattering angles of <5° (Williams and Carter, 1996) and has few geoscience
282 applications, although dark and bright bands produced by thickness variation (i.e. thickness
283 fringes) are characteristic of the wedge-shaped edges of thin samples. Z contrast imaging is much
284 more useful in geoscience and utilizes electrons that have undergone high angle (Rutherford)
285 scattering. At scattering semi-angles of >~3-5° Z contrast dominates over thickness contrast and,
286 crucially, electrons that have been Bragg scattered by crystalline material are absent. Although
287 LAADF can be used, contrast in these images may still have a contribution from Bragg scattering,
288 and so Z contrast imaging of crystalline samples is most effective using HAADF. As the intensity
289 of Rutherford scattering is proportional to $Z^{1.7-2}$ (Muller, 2009), HAADF images can be
290 qualitatively interpreted in the same way as those obtained from a SEM backscattered electron
291 detector (Figs 2, 7*a*–*b*). As the size of the probes used in modern field-emission STEM
292 instruments (typically sub-nanometre, with ~0.05 nm probes available on microscopes with
293 aberration corrected probe-forming optics; Muller, 2009) are considerably smaller than the spacing
294 of atom columns, atomic resolution HAADF images can be obtained by very fine-scale scanning
295 of the probe over a thin sample oriented with atom columns parallel to the microscope optic axis
296 (Fig. 7*c*). Atom columns scatter electrons more strongly than inter-atomic areas and so appear
297 bright (high signal intensity) in the HAADF images. Using this technique single dopant atoms in
298 synthetic materials have been detected (Muller, 2009) and as the aberration corrected STEM has a
299 very small depth of focus, by collecting through-focus images it is possible to locate individual
300 impurity atoms within amorphous and crystalline materials in three-dimensions (Xin *et al.,* 2008).
301 Owing to the Z dependence of high angle scattering, columns of atoms with different atomic
302 numbers can be recognized in HAADF images, although low Z atoms such as oxygen can be hard
303 to identify. Sample requirements for atomic resolution HAADF are stringent (clean, free of
304 preparation artifacts and <20 nm thick), although less exacting than for atomic resolution TEM
305 imaging (i.e. high-resolution HAADF is less sensitive to sample thickness and focus). In addition

306 HAADF images can be understood without the numerical simulations required to correctly
307 interpret the crystal structures seen in high-resolution TEM (Bleloch and Lupini, 2004).
308 HAADF is a very useful tool for characterizing the constituents of finely polymineralic
309 samples, especially where the minerals of interest have a significantly greater Z than their matrix.
310 Examples of such applications are locating few nanometre sized uraninite grains within
311 atmospheric aerosols (Utsunomiya and Ewing, 2003), finding ~5-10 nm sized gold nanoparticles
312 within pyrite (Palenik *et al.*, 2004) and identifying radionuclide bearing nanoparticles
313 (Utsunomiya *et al.,* 2009). Zega *et al.* (2007), Chizmadia *et al.* (2008) and Bland *et al.* (2009) have
314 also used HAADF to characterise FIB-produced foils of the very finely crystalline matrices of
315 carbonaceous chondrite meteorites, which contain Fe,Ni metal and Fe-sulphide grains embedded
316 within a lower Z silicate groundmass (Fig. 7*a*-*b*). Very fine scale mineral mixtures were studied
317 during investigation of cometary particles collected by the NASA Stardust mission (Fig. 2).
318 Atomic resolution HAADF has yet to find many applications in geoscience, but Utsunomiya *et al.*
319 (2004) showed how it could be used to help locate lead within zircon. They showed that the lead
320 was concentrated in ~5 nm sized crystalline patches (within which it had substituted for zirconium;
321 Fig. 7*c*) and had also diffused into the amorphous material of a fission track. Although potential
322 sites of lead accumulation had been located by HAADF imaging, EDX was needed to
323 unequivocally identify lead within the columns of higher Z atoms (Utsunomiya *et al.,* 2004).
324
325 *Diffraction contrast*
326 Diffraction contrast is an outcome of coherent elastic scattering of incident electrons and enables:
327 (i) discrimination of amorphous from crystalline regions within a crystal, (ii) visualisation of intra-
328 and inter-crystalline orientation differences, and (iii) identification of mineral inclusions by their
329 contrasting diffraction properties to the host crystal. As it is weak or absent in STEM images,
330 diffraction contrast imaging is mainly exploited by bright- and dark-field TEM. For incident
331 electrons to be Bragg scattered (diffracted) by a crystal, one or more sets of its lattice planes must
332 be oriented relative to the incident electron beam at the Bragg angle (typically <1º). If the crystal is
333 oriented with a major zone axis (i.e. several sets of atomic planes) parallel to the optic axis of the
334 microscope a high proportion of electrons will be Bragg scattered and so a bright-field image will
335 be dark and with little contrast. Image contrast can be increased to reveal intracrystalline
336 microtextures, or microstructures defined by local variations in orientation or unit-cell parameters
337 by tilting away from the zone axis (Fig. 8a).
338 TEM diffraction contrast imaging remains the most useful technique for high magnification
339 (although not high resolution) characterization of microstructures and microtextures (Champness,
340 1997; Putnis, 1992). Amorphous regions within a crystal can be readily identified using bright-
341 field TEM by their absence of Bragg diffraction in comparison to the crystalline host, for example
342 shock lamellae within silicate minerals from terrestrial impact craters and meteorites (e.g. Leroux,
343 2001) and amorphous layers on weathered silicates (Lee *et al.*, 2008*a*, *b*). Diffraction contrast is
344 also the primary means of imaging twins, exsolution lamellae (e.g. Brown and Parsons, 1984; Fitz
345 Gerald *et al.,* 2006) (Fig. 8a) and subgrains (Lee and Parsons, 2003; Fig. 8b). Crucially however,

346 as the Bragg angle is so small, the technique is highly sensitive to tiny (fractions of a degree)
347 intracrystalline orientation differences. These may arise due to elastic strain induced by
348 precipitates, vacancies and dislocations (e.g. Leroux, 2001) or the very-fine scale intergrowths of
349 domains formed by processes such as spinoidal decomposition (e.g. tweed orthoclase). Although
350 such orientation sensitivity can be highly beneficial, even a slight warping of the thin sample will
351 result in significant variations it the angle it makes with the incident beam so that the Bragg
352 condition may be satisfied only locally, producing 'bend contours' (Fig. 8b).
353

354 **TEM phase contrast imaging**

355 Phase contrast is present in all (S)TEM images and is formed by the interference of electron waves
356 that have been scattered by the sample and are out of phase. By optimizing phase over amplitude
357 contrast, images can be obtained that contain information on the periodicity and orientations of
358 one or more sets of atomic planes (lattice images), and that can be interpreted to reveal the
359 positions of atom columns. To form these high-resolution images the area of interest should be as
360 thin as possible (ideally <~8 nm for imaging atoms in a medium Z material at 200 kV; Williams
361 and Carter, 1996) and oriented with a zone axis precisely on the microscope's optic axis. The
362 electron beam should also be aligned to the optic axis and a relatively large objective aperture used
363 so that the image is formed from the direct beam, diffracted beams and electrons elastically and
364 inelastically scattered between them.
365 Lattice fringe imaging uses the direct beam and one or more diffracted beams and each set of
366 fringes in the image represents a set of atomic planes whose Bragg scattered electrons have been
367 accepted by the aperture. Modern TEMs can readily form such images with a <0.1 nm line
368 resolution (Smith, 2008) and the technique is not as demanding on sample thickness or defocus
369 setting as structure imaging (see below). Lattice fringe images provide detailed information on
370 local crystal structure and orientation (Fig. 9), but crucially the fringes cannot usually be
371 interpreted as direct representations of atomic planes. Nonetheless, lattice fringe imaging is used
372 extensively in geoscience, especially in studies of minerals with relatively large d-spacings such as
373 clays and phyllosilicates and a key application has been to visualize the orientation relationships of
374 the constituents of finely polycrystalline samples such as mudrocks (e.g. Peacor, 1992*a*). A good
375 example of the power of lattice fringe imaging is illustrated by Banfield and Barker (1994), who
376 were able to demonstrate that structural inheritance plays an important role in the replacement of
377 amphibole by smectite during weathering (Fig. 9).
378 In order to obtain high-resolution images that can be interpreted to reveal the locations of
379 individual atom columns or groups of columns it is necessary to use a large objective aperture that
380 accepts many diffracted beams. To simplify image interpretation, only beams diffracted from those
381 atomic planes whose d-spacings are greater than the point-to-point resolution of the microscope
382 should be used. Under these conditions images (usually series of images) can be obtained that
383 contain a representation of the crystal structure, but in order to interpret features as atoms or
384 groups of atoms it is necessary to use computer programmes to simulate the crystal structure
385 expected when looking down the relevant zone axis and given the appropriate values for defocus

386 and sample thickness (Self, 1992). This technique is used much less frequently in geoscience than
387 lattice fringe imaging due to a combination of reasons including the specialist skills and equipment
388 required to acquire and correctly interpret the results, and limitations imposed by damage to the
389 thin sample. One example is the characterization of fibrous inclusions in quartz. Ma *et al.* (2002)
390 extracted fibers from sample of rose quartz using HF acid, then by using a combination of electron
391 diffraction techniques (Fig. 10*a*), X-ray analysis and high-resolution imaging (Fig. 10*a*–*b*), they
392 found that the fibers are very similar in crystal structure and composition to dumortierite, an
393 aluminium borosilicate. It was necessary to use computer simulations to interpret correctly the
394 crystal structures observed in high-resolution TEM images (Fig. 10*a*–*b*).
395 Atomic-resolution TEM imaging is significantly limited by spherical aberrations of the
396 defocused objective (image-forming) lenses and the wavelength spread of the incident beam
397 (producing chromatic aberration). A great deal of effort has been spent on reducing the loss of
398 information by spherical aberration so that the specimen exit plane wavefunction (EPWF) can be
399 reconstructed or retrieved. Successful application of these techniques can yield sub-Ångstrom (i.e.
400 <0.1 nm) resolution images whereby the positions of atoms can be measured to precisions of tens
401 of picometres (Hetherington, 2004; Houben *et al.,* 2006; Urban, 2008, 2009). One method is to
402 acquire a series of 10-20 images at slightly different levels of objective lens defocus, each of
403 which will contain a subtly different set of aberrations (Kirkland and Meyer, 2004). By
404 computationally processing each aberrated image the EPWF can be reconstructed and atomic
405 resolution images produced. The other way to reduce spherical aberration is to introduce lenses
406 into the microscope column that effectively 'reverse' aberrations imposed by the objective lens.
407 Single images containing readily interpretable atomic positions may be obtained using aberration
408 corrected TEMs (Kirkland *et al.,* 2008), and although EPWF reconstruction techniques are still
409 often required they are computationally more straightforward than for images obtained using non-
410 corrected microscopes (Kirkland and Meyer, 2004; Urban, 2008, 2009). The driver for sub-
411 Ångstrom resolution imaging has been characterization of advanced functional materials such as
412 superconductors (Urban, 2009) and these techniques are unlikely to see widespread use in
413 geoscience, especially given the stringent requirements for the thickness of a sample and its
414 stability under the high current densities used for illuminating very small sample volumes.
415
416 **(S)TEM electron diffraction**
417 Diffraction patterns record the angular distribution of electrons that have been coherently
418 elastically scattered by the thin sample and by <~3°. Amorphous materials produce patterns with
419 diffuse intensity variations whereas single crystals yield periodic arrays of spots generated by
420 Bragg scattering. Spot patterns are effectively a two dimensional section through the reciprocal
421 lattice of the crystal and the positions of spots are determined by the separation (d-spacing) of
422 atomic planes and their orientation. The TEM based technique of selected area electron diffraction
423 (SAED) is used most widely in geoscience, but other methods including precession electron
424 diffraction, convergent beam electron diffraction and electron nanodiffraction have specific
425 applications.

426 For SAED the foil is illuminated using a broad and parallel electron beam and the region
427 from where the diffraction pattern is required is defined using the selected area aperture; the
428 smallest area selectable is ~500 nm in diameter. If one crystal is present, and oriented with several
429 sets of atomic planes (i.e. a zone axis) at the Bragg angle relative to the incident beam, a single
430 array of spots is formed (Fig. 1*b*). A SAED pattern from two or more crystals will yield
431 superimposed patterns and a region containing many crystals in random orientations relative to
432 each other will generate a large number of spots that merge into continuous rings (Fig. 1*b*). In
433 geoscience SAED is used most commonly to: (i) to help identify minerals and (ii) determine the
434 orientation of the thin sample and the crystallographic orientations of grain boundaries and
435 intracrystalline features including dislocations, twin composition planes and exsolution lamellae.
436 Minerals can be identified using the spacings of spots, supported by information on the
437 angles between diffracting planes, and pattern symmetry of can also provide a guide to the crystal
438 system. SAED is inferior to X-ray diffraction (XRD) in the accuracy and precision of d-spacing
439 measurements. However, with careful calibration of the camera factor (essentially the
440 magnification of the SAED pattern) and correction for elliptical distortion, accuracies and
441 precisions of 0.1% in d-spacing determinations can be achieved (Steeds and Morniroli, 1992;
442 Mugnaioli *et al.* 2009). For such work it is desirable to deposit a standard such as sputtered gold
443 onto the thin sample to give rings of known d-spacing superimposed on the diffraction pattern of
444 the sample. Mugnaioli *et al.* (2009) note that although an accuracy of 0.1% is achievable, d-
445 spacings of any one crystal may vary by > 0.1% owing to intracrystalline compositional
446 heterogeneities; dehydration under vacuum and ion and electron beam damage may also modify
447 the original d-spacings of minerals including micas and phyllosilicates. To determine the
448 approximate orientations of features in an image, crystallographic directions obtained from an
449 indexed SAED pattern are plotted on its corresponding image (after correction for any magnetic
450 rotation between the two). However, in order to establish the absolute orientation 'trace analysis'
451 needs to be undertaken using several diffraction pattern-image pairs (e.g. Loretto, 1994).
452 Recently a variant of SAED termed precession electron diffraction (PED) has become
453 commercially available and enables a much more sophisticated interpretation of spot patterns
454 derived from single crystals. PED requires a modified TEM and is undertaken by precessing the
455 electron beam around the optic axis of the microscope (Jacob *et al.*,, 2009). The resulting patterns
456 contain spots whose intensities (in addition to d-spacings and angles) can be used to undertake
457 sophisticated crystallographic analysis including crystal structure determinations and assessment
458 of bonding (Avilov *et al.,* 2007). Electron crystallography by PED offers a clear advantage over X-
459 ray crystallography because structure determinations can be done on much smaller crystals than
460 can be effectively studied by X-ray diffraction (Avilov *et al.,* 2007). Although few suitably
461 equipped microscopes are currently available, the ease of use of PED coupled with the detailed
462 information it can provide, mean that it is likely to find many future applications in mineralogy
463 (e.g. Jacob *et al.,* 2009). Convergent beam electron diffraction (CBED) patterns are best acquired
464 from crystals with a low defect density and are formed using a focused electron probe (and a large
465 condenser aperture) so that the size of the diffracting volume is essentially determined by the

466 dimensions of the electron beam. Thus, CBED patterns can be obtained from ~10 nm sized
467 regions. The patterns contain discs of intensity, as opposed to the spots of SAED, and the structure
468 of the discs contains a wealth of crystallographic information unobtainable by conventional SAED
469 including point and space group (Steeds and Morniroli, 1992), and CBED also enables crystal
470 structure refinements (e.g. Beermann and Brockamp, 2005). Using the very small probe available
471 in STEM, electron nanodiffraction (END) patterns can be acquired from sub-nanometre sized
472 regions of a sample (Cowley, 2004). These patterns again contain discs of intensity rather than
473 sharp spots (Fig. 11), but are indexed in the same way as SAED patterns. Janney *et al.* (2000,
474 2001) estimated that the error in determination of unit-cell dimensions by END was <~5%. By
475 scanning the probe over the sample and acquiring END patterns at each point, this technique can
476 be used to obtain nanoscale structural information (Janney *et al.,* 2000, 2001). A drawback of
477 END is that the crystals cannot be tilted during experiments so that many of the patterns acquired
478 from a polycrystalline sample will not be oriented precisely on a zone axis. As with all work using
479 a fine probe, electron beam damage is a severe limitation and kaolinite for example can turn
480 amorphous in less than one second (Fig. 11).
481 Geoscientists are now also making extensive use of Fourier transforms of high-resolution
482 (S)TEM images to obtain information on orientations and spacings of atomic planes. This
483 technique converts the periodicity of a high-resolution digital image into a diffractogram that can
484 be indexed in the same way as a SAED pattern to: (i) help identify minerals (e.g. Palenik *et al.,*
485 2004; Utsunomiya *et al.* 2009), (ii) confirm orientation data derived from the source image (e.g.
486 Utsunomiya *et al.* 2004; Chizmadia and Brearley, 2008) and (iii) to assess crystallinity (Benzerara
487 *et al.,* 2005). Diffractograms are useful because they greatly reduce the complexity of the high-
488 resolution image and so can reveal features that are hard to identify visually, but in doing so
489 information may be lost and so they are not a replacement for conventional diffraction work.
490

491 **Limitations to (S)TEM work by electron beam damage**

492 Even before (S)TEM work is undertaken, minerals may be modified by exposure to a vacuum in
493 the ion mill, coater and (S)TEM. For example, smectite commonly dehydrates with a consequent
494 change its (001) layer spacings from ~1.5-1.2 nm to ~1.0 nm. The deleterious effects of ion
495 bombardment were described earlier, and electron beam irradiation can further alter thin samples
496 and by three mechanisms: radiolysis, heating and knock-on (or displacement) damage (Williams
497 and Carter, 1996; Egerton *et al.,* 2004) (Fig. 12). For many minerals, electron induced sample
498 deterioration can be the principal limitation to the spatial resolution at which (S)TEM images, and
499 EDX and EELS spot analyses and maps can be acquired.
500 Radiolysis is the ionization of sample atoms during inelastic scattering and leads to breaking
501 of bonds, resulting in defect formation and amorphisation, sputtering of atoms from sample
502 surfaces and changes in chemistry (Fig. 12). Heating also takes place as energy is transferred from
503 incident electrons to sample atoms during inelastic scattering, and can be a particular problem for
504 minerals with poor thermal conductivity (Egerton *et al.,* 2004). Breaking of bonds, vaporization
505 and chemical reactions including recrystallization are common consequences of heating (Fig. 12).

506 Silicate minerals are very prone to radiolysis and heating, but its effects may be minimised by
507 cooling the sample using liquid nitrogen or increasing accelerating voltage (Williams and Carter,
508 1996) in addition to using a broader beam (in TEM mode), or rastered beam (in STEM mode) and
509 reducing acquisition times for images, diffraction patterns and analyses. Knock-on damage is
510 mainly a consequence of momentum transfer from incident electrons to atomic nuclei during high-
511 angle elastic scattering, which despite the term 'elastic' does involve some energy loss to incident
512 electrons. This process can lead to displacement of internal atoms, especially those of low Z, and
513 sputtering of the more weakly bonded atoms from sample surfaces (Williams and Carter, 1996;
514 Egerton *et al.,* 2004) (Fig. 12). As the magnitude of knock-on damage increases with accelerating
515 voltage and decreases with Z and strength of atomic bonds, it can be countered by reducing kV to
516 below the displacement threshold of sample atoms, which is >200 kV for atoms of medium to high
517 Z, although those close to the sample surface will have a lower threshold (Egerton *et al.*, 2004).
518 The susceptibility of a given sample to damage will depend on the dominant damage
519 mechanism(s) operative within the mineral of interest and under the instrumental conditions used.
520 However, beam damage is typically severe in hydrous minerals and those that are alkali-rich,
521 including feldspars (e.g. Janney and Wenk 1999; Lee *et al.,* 2007) and the readily identifiable
522 consequences are defect formation, amorphisation, 'drilling' of holes (Fig. 7*a–b*) and changes in
523 chemical composition (see later). Carbonates are also unstable (Reeder, 1992), and in particular
524 those containing ions that have substituted for Ca^{2+} (Barber and Wenk, 1984), leading to the
525 formation of dislocations and bubbles. At greater degrees of damage carbonates can lose CO_2, with
526 calcite recrystallizing to CaO (lime) and dolomite recrystallizing to CaO plus MgO, probably in
527 response to ionization of carbonate anions (Cater and Buseck, 1985). Lee (1993) found that
528 gypsum ($CaSO_4.2H_2O$) readily recrystallizes in the TEM, producing hemihydrite ($CaSO_4.0.5H_2O$),
529 anhydrite ($CaSO_4$) and finally lime (CaO) over the space of a few minutes observation at 200 kV.
530 This change in crystal structure indicates progressive loss of H_2O, but as EDX showed that the
531 Ca/S ratio also increased, SO_2 must have been liberated (Lee, 1993). S.Lee *et al.* (2007) found that
532 damage can also cause kaolinite to recrystallize to polycrystalline silica as a consequence of
533 breakage and reforming of Si-O bonds. Utsunomiya *et al.* (2009) give a very good account of the
534 problems in trying to characterize environmental nanoparticles, some of which were extremely
535 unstable under the electron beam.
536 Another electron beam-induced artifact, which is especially problematic during EDX and
537 EELS work, is hydrocarbon contamination (Fig. 12). Hydrocarbon molecules may be deposited
538 during ion milling and coating, or derived from vapour present in the microscope column, and are
539 polymerized on the sample surface by the electron beam. This contamination can be mitigated by
540 plasma cleaning the sample and holder prior to (S)TEM work, heating/cooling the sample, or by
541 rastering the beam over the area of interest to 'burn' away the hydrocarbons.
542
543 **Compositional analysis by (S)TEM**
544 Incident electrons that interact with the electron clouds surrounding sample atoms are inelastically
545 scattered and in the process change direction (by <~1°) and lose up to ~5% of their energy.

546 Inelastic scattering provides most of the information in EELS spectra and by exciting sample
547 atoms also generates the X-rays for EDX. The EDX and EELS techniques both enable qualitative
548 and quantitative determination of elemental compositions, but EELS additionally yields
549 information on bonding and valence states. EDX analysis of thin samples is a mature and well
550 understood technique (Peacor 1992b) and geoscientists with experience of analytical SEM or
551 EPMA will be able to acquire and interpret (S)TEM X-ray analyses with little difficulty. EELS by
552 contrast is a far more specialist method, but a very powerful tool for certain applications (Buseck
553 and Self, 1992; Garvie *et al.,* 1994; Egerton, 2009).
554
555 *X-ray analysis*
556 Bremsstrahlung and characteristic X-rays produced during ionization of specimen atoms can be
557 collected and their energies analysed *via* an energy-dispersive X-ray detector above the thin
558 sample (Fig. 4). (S)TEM-EDX differs from microanalysis of bulk materials in two important
559 respects: (i) 100-300 kV incident electrons will generate much higher energy X-rays than 20-30
560 kV electrons employed by SEM/EPMA and (ii) the volume of the sample from which X-rays are
561 generated is far smaller than in a bulk material, which is a consequence of their thickness, the
562 small incident beam diameter (quantitative analyses can be acquired from suitable samples using a
563 ~10 nm beam from a thermionic gun and a ~1 nm beam from a FEG; Williams and Carter, 1996)
564 and high electron energies (spreading of the electron beam by scattering increases with decreasing
565 electron energy and with $t^{0.66}$). Spot analyses can be obtained in TEM and STEM modes although
566 element maps and spectrum maps (in which each pixel contains all the information of an emission
567 spectrum) require STEM (Fig. 2).
568 Quantitative elemental analysis by (S)TEM-EDX is simpler than for bulk materials because
569 in appropriately thin samples X-ray absorption and fluorescence can be essentially ignored (i.e. the
570 thin samples are effectively transparent to X-rays generated within them). This is called the 'thin
571 film criterion' (Cliff and Lorimer, 1975). As described by Peacor (1992*b*), (S)TEM-EDX can
572 achieve detection limits of ~0.1 wt% and yield concentrations within error of those acquired from
573 bulk samples of the same materials using EPMA. If the samples are thicker than ~50-100 nm
574 and/or low Z elements (which produce low energy X-rays) are of interest, then the thin film
575 criterion breaks down and corrections for absorption, and possibly fluorescence, must be
576 incorporated in quantification procedures (Williams and Carter, 1996). (S)TEM-EDX has been
577 used widely in geoscience and in particular for studying fine-grained rocks such as shales and
578 slates and their constituent clays and phyllosilicates, which can have considerable inter- and
579 intracrystalline compositional variation.
580 Optimising instrumental conditions for quantitative (S)TEM-EDX requires a trade-off
581 between competing variables. In the thinnest samples electron beam spreading will be at a
582 minimum, giving the highest spatial resolutions for a given probe size, but X-ray count rates will
583 be correspondingly low, possibly necessitating relatively long counting times so that specimen
584 drift (typically ~0.5 nm min^{-1}), electron beam damage and carbon contamination may cause
585 significant problems. Damage to the sample is identifiable by hole drilling (Fig. 7*a*–*b*), although

586 element loss will occur before this is observed. For example, during STEM-EDX analysis of
587 muscovite and paragonite, Peacor (1992b) noted the loss by diffusion of K, Na and Al relative to
588 Si and Lee *et al.* (2007) also found rapid loss of Na and K during analysis of alkali feldspar.
589 Janney and Wenk (1999) discuss the problems in obtaining quantitative analyses of plagioclase
590 feldspar and the merits of various mitigation strategies including rastering the electron beam (in
591 STEM mode), undersaturating the electron source and cooling the specimen with liquid nitrogen.
592 Beam damage can also be alleviated by analysing thicker regions of the sample (if available),
593 which will have the additional advantage of giving greater count rates, although electron scattering
594 will increase, thus limiting spatial resolution, and absorption and fluorescence corrections may
595 have to be incorporated into quantification routines. Importantly, (S)TEM-EDX work can also
596 suffer from spurious X-rays (i.e. those derived from outside of the volume from which the analysis
597 is sought, typically the holder or even microscope components) and analyses of thin samples may
598 also contain X-rays from elements implanted during milling (e.g. argon and gallium).
599
600 *EELS*
601 EELS quantifies the energy lost by incident electrons during ionization of sample atoms
602 accompanying inelastic interactions, and losses range from ~5 eV to 2 KeV. The EELS detector is
603 positioned beneath the sample to collect unscattered and low angle (<1º) scattered electrons and
604 using a magnetic prism (Fig. 4) separates them according to the energy they have lost. EELS
605 measurements can be obtained by TEM or STEM, although STEM offers the significant advantage
606 that analytical work can be undertaken in parallel with LAADF/HAADF imaging. The spectra
607 obtained can be used for qualitative and quantitative analysis of elemental abundances and
608 determination of valence states and bonding of sample atoms.
609 An EELS spectrum contains three energy loss regions: (i) the zero loss peak (<5 eV), which
610 contains the direct beam and electrons that have undergone scattering but lost little energy, (ii) the
611 low loss region (5 to 50 eV) representing ionization of outer shell electrons of specimen atoms,
612 and (iii) the high loss region (50 to ~2000 eV) produced by excitation of inner shell (core)
613 electrons. The high loss region comprises a small proportion (~5%) of the net intensity of the
614 spectrum but contains a series of sharp increases in energy loss called 'edges'. The energy loss of
615 the edge is indicative of the element present, and information on bonding and valence states comes
616 from subtle changes in the energy loss and the fine structure of the 30-50 eV long tail to the edge
617 (Garvie *et al.,* 1994). As the intensity of the core edge of a given element is a function of the
618 number of its atoms that are present in the illuminated volume, EELS can be used to quantify
619 elemental compositions. Considerable processing may be required in order to identify edges
620 against the background and quantify their intensities (Fig. 13), but reliable data can be obtained.
621 For example, Garvie and Buseck (2004) determined concentrations of oxygen, nitrogen and
622 sulphur in <100 nm sized carbonaceous nanospheres and nanotubes from the Tagish Lake
623 (carbonaceous chondrite) meteorite. Using the energy loss of the carbon edge and its fine structure,
624 they were also able to show that the carbon had long-range order and was bonded to oxygen,
625 nitrogen and sulphur. Detailed information on Si-O bonding in crystalline and amorphous silicates

626 has also been obtained by analysis of the silicon core loss edge (Garvie and Buseck, 1999; Fig.
627 13).
628 EELS has been used extensively for determining valence states of elements within minerals
629 at the few nanometre scale. Elements studied include manganese (e.g. Buseck and Self, 1992;
630 Garvie and Craven, 1994; Loomer *et al.*, 2007), iron (e.g. Garvie and Buseck, 1998; Heard *et al.,*
631 2001; Zega *et al.,* 2003; Garvie *et al.,* 2004) (Fig. 14), chromium (Garvie *et al.,* 2004) and cerium
632 (Utsunomiya *et al.*, 2007). Garvie and Buseck (1998) first demonstrated that the L_3 edges of Fe^{2+}
633 and Fe^{3+} were sufficiently different (~1 eV) that iron valence states could readily be determined.
634 By measuring the relative heights of the two peaks the $Fe^{3+}/\Sigma Fe$ values of mixed valence minerals
635 could also be quantified (Zega *et al.,* 2003; Garvie *et al.,* 2004). Loomer *et al.* (2007) used the
636 energy of the Mn L_3 edge and relative intensities of the Mn L_3 and L_2 edges to determine average
637 manganese valence states, although were unable to distinguish Mn^{3+} from Mn^{2+} and Mn^{4+}.
638 Using STEM, EELS analyses can be acquired at spatial resolutions of <1 nm, which is
639 superior to the resolution of STEM-EDX under comparable conditions, although such fine-scale
640 analyses can be obtained from only those materials that are sufficiently stable to withstand the
641 high beam currents required to generate a usable signal from such small volumes. By acquiring
642 spectra from grids of closely spaced points in STEM mode (i.e. spectrum mapping), images can be
643 constructed to show spatial variations in elemental abundances or even valence states. For
644 example, Loomer *et al.* (2007) mapped the distribution of manganese with different valence states
645 in the Mn-rich minerals braunite and bementite by acquiring a spectrum map over a 300 by 150
646 nm area at a 5 nm point spacing (and with a comparably sized probe), which took 17 minutes. The
647 acquisition times for large spectrum maps may be considerable, over which timescales the sample
648 is likely to have drifted significantly (although automatic drift correction can be used). EELS
649 acquisition times are much shorter in aberration corrected microscopes, but sample damage may
650 be severe (Muller, 2009). Garvie *et al.* (2004) undertook a quantitative study of the effect of
651 electron beam damage on EELS analyses of the phyllosilicate mineral cronstedtite. They found
652 that under the experimental configuration used beam damage led to loss of H with a corresponding
653 increase of $Fe^{3+}/\Sigma Fe$ over their true values. It is again important to note that a significant
654 proportion of the volume of a sample sufficiently thin for good EELS work will be close to its
655 surface so that if near-surface regions have been compositionally modified during ion milling,
656 obtaining information on the elemental composition, valence and bonding that is a true reflection
657 of the original mineral may be challenging.
658
659 *Energy-filtered TEM (EFTEM) imaging*
660 EFTEM uses electrons from a specific region of the EELS spectrum to form an image, for
661 example the zero loss peak or one or more core loss edges. Those images formed using the zero-
662 loss peak will be free of inelastically scattered electrons and so this technique is especially useful
663 for studying thick samples, TEM images from which would otherwise suffer significantly from
664 chromatic aberration. Using the core loss edges enables chemical imaging and this method has the
665 major advantage over point-by-point X-ray or EELS mapping that the images can be acquired

666 rapidly (seconds to a few minutes) and with sub-nanometre spatial resolutions (Grogger *et al.,*
667 2003). EFTEM chemical imaging has been used in applications including characterizing finely
668 polymineralic acid mine drainage samples (Hochella *et al.*, 1999), observing oxygen enrichment in
669 the rims of meteoritic Fe,Ni metal grains (Chizmadia *et al.*, 2008) and mapping the distribution of
670 manganese and iron within desert varnish (Garvie *et al.*, 2008) (Fig. 15). Moore *et al.* (2001)
671 demonstrated how EFTEM could be used to differentiate augite from pigeonite *via* contrasts in
672 intensity of images acquired using Mg, Ca and Fe core loss edges; a difference between the two
673 minerals of 2 atomic % magnesium was readily resolvable. Zhang and Veblen (2007) also showed
674 how EFTEM could be used to identify few nanometre sized regions of Ca-depletion and Fe-
675 enrichment at deformation twin boundaries in augite. The downside of EFTEM imaging is that
676 electron beam damage to the very thin samples can be severe, especially as high beam currents are
677 needed to obtain sufficient signal intensities from the narrow regions of the EELS spectra that
678 contain core loss edges.
679
680 **Low voltage and wet STEM**
681 It has recently become possible to acquire images of thin samples using unscattered and scattered
682 electrons in a FEG-SEM. As the incident electrons are in a small (few nanometre) probe that is
683 rastered over the sample to form an image this is a STEM technique, and the prefix 'low voltage'
684 (LV) denotes the 30 kV maximum accelerating voltage of most SEMs. Images are formed using
685 electron detectors positioned a few millimetres beneath the thin sample and a variety of detector
686 configurations are currently available. The simplest uses a pair of diodes, essentially an inverted
687 backscattered electron detector (Lee and Smith, 2006). The diode immediately beneath the thin
688 sample will intercept the direct beam and a proportion of the scattered electrons (i.e. a form of
689 bright-field image) whereas the offset diode will form a dark-field image from electrons scattered
690 at high angles and in the appropriate direction (i.e. similar to HAADF STEM). The more
691 sophisticated detectors have a bright-field diode beneath the sample and an annular dark-field
692 detector some distance further below. In some systems the separation of the dark-field detector
693 from the sample can be modified to change collection semi-angles, which can be up to tens of
694 degrees (van Ngo *et al.,* 2007). LV-STEM clearly has significant limitations in comparison to
695 conventional high voltage (S)TEM, including: (i) the inability to acquire electron diffraction
696 patterns means that orientation data cannot be obtained, (ii) image interpretation is complicated by
697 the variable contributions of both diffraction contrast and Z contrast, depending on relative
698 positions of thin samples and detectors (Lee and Smith, 2006), and (iii) there is only a very limited
699 capability to tilt the samples. One advantage over conventional high-voltage STEM is that the
700 lower accelerating voltages used mean that the intensity of scattering is greater, potentially giving
701 images with superior Z contrast, and at 30 kV knock-on damage will be essentially absent.
702 LV-STEM is a technique with significant potential in geoscience because its functions are
703 integrated with the controls of the SEM, an instrument with which most geoscientists are familiar,
704 and it enables acquisition of images and X-ray analyses of considerably higher spatial resolutions
705 than obtainable from bulk samples (Lee and Smith, 2006). Bright-field LV-STEM is very effective

for imaging the morphology of particles dispersed on a carbon film, for example clay mineral crystals (Fig. 16*a–b*) and environmental samples such as atmospheric aerosols. Dark-field imaging works well for polymineralic samples that vary little in thickness (i.e. prepared by FIB or ultramicrotome) so that Z contrast dominates the dark-field signal and such images are complementary to those obtained by TEM (Fig. 16*c*), and can be comparable to STEM HAADF images acquired at the same magnification (Fig. 16*d*). Some LV-STEM images can contain considerable diffraction contrast enabling individual crystals of polycrystalline samples and strain fields around dislocations to be imaged (Lee and Smith, 2006). Van Ngo *et al.* (2007) have even demonstrated that lattice images of carbon nanotubes (spacing 0.34 nm) can be obtained by bright-field LV-STEM, albeit using an ultra-high resolution cold field emission SEM with immersion optics. X-ray spectra and maps of the thin samples are readily obtainable by SEM-EDX (e.g. Zega *et al.,* 2007; Hay *et al.*, 2009) and although count rates are very low, the spatial resolution of the analyses is high owing to the small interaction volumes. Acquiring good EDX analyses of thin samples when in LV-STEM holders can be considerably more difficult because the holders themselves may shield the thin sample from the X-ray detector and spurious X-rays are produced by copper grids, the sample holder and the electron detectors.

LV-STEM in an environmental SEM can be used to study materials whilst in the stability field of liquid water (Bogner *et al.*, 2005) and images can even be acquired from a liquid film several micrometres thick (Bogner *et al.*, 2007). Although still in its infancy, there is considerable potential for 'wet-STEM' in geomicrobiology, for example imaging the aggregation of nanoparticles in aqueous suspension.

Conclusions

The message of this review is that the enormous potential of (S)TEM techniques for characterization of Earth and planetary materials is now readily accessible to the geoscientist. This is partly due to advancements in sample preparation, in particular the FIB technique, but also reflects the development of technologies including Z-contrast HAADF imaging and spectrum mapping using X-rays and electrons. Even the LV-STEM technique will give the geoscientist some of the advantages of thin sample analysis (e.g. high spatial resolution X-ray analysis) without the cost of conventional (S)TEM work. There are many other highly sophisticated (S)TEM based techniques that this review has not described, but have specialist applications. These include electron tomography, which enables reconstruction of the three-dimensional structure of nanoscale particles using sequences of two-dimensional images (e.g. Midgley and Weyland, 2003; Friedrich *et al.*, 2005; Midgley and Dunin-Borkowski, 2009) and electron holography, which has enabled new insights into the magnetic microstructure of minerals (e.g. Feinberg *et al.,* 2006; Midgley and Dunin-Borkowski, 2009).

Acknowledgements

I would like to thank Professor Alan Craven (Department of Physics and Astronomy, Glasgow University) for access to FIB and TEM facilities of the Kelvin Nanocharacetrisation Center, Billy Smith, Brian Miller and Colin How for their technical assistance and Ian MacLaren and Maureen MacKenzie for helpful discussions. I am also grateful to Laurence Garvie for kindly supplying the EFTEM image and to David Barber, David Brown, Ian Parsons and Caroline Smith for their support. I also thank John Fitz Gerald and an anonymous reviewer for their constructive comments on the manuscript.

Glossary

ADF	Annular dark-field
CBED	Convergent beam electron diffraction
EBSD	Electron backscatter diffraction
EDX	Energy dispersive X-ray analysis
EELS	Electron energy loss spectroscopy
EFTEM	Energy filtered transmission electron microscopy
END	Electron nanodiffraction
EPMA	Electron probe microanalysis
EPWF	Exit plane wavefunction
FEG	Field-emission gun
FIB	Focused ion beam
HAADF	High angle annular dark-field
HRTEM	High-resolution transmission electron microscopy
LAADF	Low angle annular dark-field
LV-STEM	Low voltage scanning transmission electron microscopy
PED	Precession electron diffraction
SAED	Selected area electron diffraction
SEM	Scanning electron microscopy
SEM-EDX	Scanning electron microscopy-energy dispersive X-ray analysis
STEM	Scanning transmission electron microscopy/microscope
(S)TEM	Both scanning transmission electron microscopy and transmission electron microscopy
(S)TEM-EDX	Scanning transmission electron microscopy-energy dispersive X-ray analysis
TEM	Transmission electron microscopy/microscope
XRD	X-ray diffraction
Z	Atomic number

786 **References**

787 Avilov, A., Kuligin, K., Nicolopoulos, S., Nickolskiy, M., Boulahya, K., Portillo, J., Lepeshov, G.,
788 Sobolev, B., Collette, J. P., Martin, N., Robins, A.C. Fischione, P. (2007) Precession
789 technique and electron diffractometry as new tools for crystal structure analysis and chemical
790 bonding determination. *Ultramicroscopy*, **7**, 431–444.
791 Barber, D.J. (1970) Thin foils of non-metals made for electron microscopy by sputter-etching.
792 *Journal of Materials Science,* **5**, 1–8.
793 Barber, D.J. (1981) Demountable polished extra-thin sections and their use in transmission
794 electron microscopy. *Mineralogical Magazine,* **44**, 357–359.
795 Barber, D.J. (1993) Radiation damage in ion-milled specimens: Characteristics, effects and
796 methods of damage mimitation. *Ultramicroscopy,* **52**, 101–125.
797 Barber, D.J. and Wenk, H-R (1984) Microstructures in carbonates from the Alno and Fen
798 carbonatities. *Contributions to Mineralogy and Petrology*, **88**, 233–245.
799 Banfield, J.F. and Barker, W.W. (1994) Direct observation of reactant-product interfaces formed
800 in natural weathering of exsolved, defective amphibole to smectite: Evidence for episodic,
801 isovolumetric reactions involving structural inheritance. *Geochimica et Cosmochimica Acta*,
802 **58**, 1419-1429.
803 Barker, W.W. and Banfield, J.F. (1996) Biologically versus inorganically mediated weathering
804 reactions: Relationships between minerals and extracellular microbial polymers in
805 lithobiontic communities. *Chemical Geology*, **132**, 55–69.
806 Beermann, T and Brockamp, O. (2005) Structure analysis of montmorillonite crystallites by
807 convergent-beam electron diffraction. *Clay Minerals*, **40**, 1-13.
808 Benzerara, K., Menguy, N., Guyot, F., Vanni, C. and Gillet, P. (2005) TEM study of a silicate-
809 carbonate-microbe interface prepared by focused ion beam milling. *Geochimica et*
810 *Cosmochimica Acta,* **69**, 1413–1422.
811 Bland, P.A., Jackson, M.D., Coker, R.F., Cohen, B.A., Webber, J.B.W., Lee, M.R., Duffy, C.M,
812 Chater, R.J., Ardakani, M.G., McPhail, D.S., McComb, D.W. and Benedix, G.K. (2009)
813 Why aqueous alteration in asteroids was isochemical: High porosity ≠ high permeability.
814 *Earth and Planetary Science Letters* (in press).
815 Bleloch, A. and Lupini, A. (2004) Imaging at the picoscale. *Materials Today*, **7**, 42.
816 Benzerara, K., Menguy, N., Guyot, F., Vanni, C. and Gillet, P. (2005) TEM study of a silicate-
817 carbonate-microbe interface prepared by focused ion beam milling. *Geochimica et*
818 *Cosmochimica Acta*, **69**, 1413–1422.
819 Bogner, A., Thollet, G., Basset, D., Jouneau, P-H and Gauthier, C. (2005) Wet STEM: A new
820 development in environmental SEM for imaging nano-objects included in a liquid phase.
821 *Ultramicroscopy,* **104**, 290–301.
822 Bogner, A., Jouneau, P.H., Thollet, G., Basset, D. and Gauthier, C. (2007) A history of scanning
823 electron microscopy developments: Towards "wet-STEM" imaging. *Micron*, **38**, 390–401.
824 Bradley, J.P. and Brownlee D.E. (1986) Cometary particles – thin sectioning and electron-beam
825 analysis. *Science*, **231**, 1542–1544.

826 Bonneville, S., Smits, M.M., Brown, A., Harrington, J., Leake, J.R., Brydson, R. and Benning,
827 L.G. (2009) Plant-driven fungal weathering: Early stages of mineral alteration at the
828 nanometer scale. *Geology*, **37**, 615–618.
829 Brown, W.L. and Parsons, I. (1984) Exsolution and coarsening mechanisms and kinetics in an
830 ordered cryptoperthite series. *Contributions to Mineralogy and Petrology*, **86**, 3-18.
831 Buseck, P.R. (1992) *Minerals and reactions at the atomic scale: Transmission electron*
832 *microscopy.* Reviews in Mineralogy **27**, Mineralogical Society of America, 516 pp.
833 Buseck, P.R. and Self, P. (1992) Electron energy-loss spectroscopy (EELS) and electron
834 channeling (ALCHEMI). Pp 141–180 in: *Minerals and reactions at the atomic scale:*
835 *Transmission electron microscopy* (P.R. Buseck, editor). Reviews in Mineralogy **27**,
836 Mineralogical Society of America.
837 Casey, W.H., Westrich, H.R., Massis, T., Banfield, J.F. and Arnold, G.W. (1989) The surface of
838 labradorite feldspar after acid hydrolysis. *Chemical Geology,* **78**, 205–218.
839 Cater, E.D. and Buseck, P.R. (1985) Mechanisms of decomposition of dolomite, $Ca_{0.5}Mg_{0.5}CO_3$, in
840 the electron microscope. *Ultramicroscopy*, **18**, 241–252.
841 Champness, P.E. (1977) Transmission Electron Microscopy in Earth Science. *Annual Review of*
842 *Earth and Planetary Sciences*, **5**, 203-226.
843 Chizmadia, L.J. and Brearley, A.J. (2008) Mineralogy, aqueous alteration, and primitive textural
844 characteristics of fine-grained rims in the Y-791198 CM2 carbonaceous chondrite: TEM
845 observations and comparison to ALHA81002. *Geochimica et Cosmochimica Acta*, **72**, 602–
846 625.
847 Chizmadia, L.J., Xu, Y., Schwappach, C. and Brearley, A.J. (2008) Characterisation of micron-
848 sized Fe,Ni metal grains in fine-grained rims in the Y-791198 CM2 carbonaceous chondrite:
849 Implications for asteroidal and preaccretionary models of aqueous alteration. *Meteoritics and*
850 *Planetary Science,* **43**, 1419–1438.
851 Cliff, G. and Lorimer, G.W. (1975) Quantitative-analysis of thin specimens. *Journal of*
852 *Microscopy*, **103**, 203–207.
853 Cowley, J.M. (2004) Applications of electron nanodiffraction. *Micron*, **35**, 345–360.
854 Egerton, R.F., Li, P. and Malac, M. (2004) Radiation damage in the TEM and SEM. *Micron,* **35**,
855 399–409.
856 Egerton, R.F. (2009) Electron energy-loss spectroscopy in the TEM and SEM. *Reports on*
857 *Progress in Physics*, **72,** 016502.
858 Feinberg, J.M., Harrison, R.J., Kasama, T., Dunin-Borkowski, R.E., Scott, G.R. and Renne, P.R.
859 (2006), Effects of internal mineral structures on the magnetic remanence of silicate-hosted
860 titanomagnetite inclusions: An electron holography study, *Journal of Geophysical Research*,
861 **111**, B12S15.
862 Fitz Gerald, J.D., Parsons, I. and Cayzer, N. (2006) Nanotunnels and pull-aparts: Defects of
863 exsolution lamellae in alkali feldspars. *American Mineralogist*, **91**, 772-783.

864 Friedrich, H., McCartney, M.R. and Buseck, P.R. (2005) Comparison of intensity distributions in
865 tomograms from BF TEM, ADF STEM, HAADF STEM, and calculated tilt series.
866 *Ultramicroscopy*, **106**, 18–27.
867 Garvie, L.A.J. and Craven, A.J. (1994) High-resolution parallel electron-energy-loss spectroscopy
868 of Mn $L_{(2,3)}$-edges in inorganic manganese compounds. *Physics and Chemistry of Minerals*,
869 **21**, 191-206.
870 Garvie, L.A.J. and Buseck, P.R. (1998) Ratios of ferrous to ferric iron from nanometre-sized areas
871 in minerals. *Nature*, **396**, 667–670.
872 Garvie, L.A.J. and Buseck, P.R. (1999) Bonding in silicates: Investigation of the Si $L_{2,3}$ edge by
873 parallel electron energy-loss spectroscopy. *American Mineralogist*, **84**, 946–964.
874 Garvie, L.A.J., Craven, A.J. and Brydson, R. (1994) Use of electron energy-loss near-edge fine-
875 structure in the study of minerals. *American Mineralogist*, **79**, 411-425
876 Garvie, L.A.J., Zega, T. J., Rez, P. and Buseck, P.R. (2004) Nanometer-scale measurements of
877 $Fe^{3+}/\Sigma Fe$ by electron energy-loss spectroscopy: A cautionary note. *American Mineralogist*,
878 **89**, 1610–1616.
879 Garvie, L.A.J., Burt, D.M. and Buseck, P.R. (2008) Nanometer-scale complexity, growth, and
880 diagenesis in desert varnish. *Geology*, **36**, 215–218.
881 Grogger, W., Schaffer, B., Krishnan, K. M. and Hofer, F. (2003) Energy-filtering TEM at high
882 magnification: spatial resolution and detection limits. *Ultramicroscopy* **96,** 481–489.
883 Hay, D.C., Dempster, T.J., Lee, M.R. and Brown, D.J. (2009) Anatomy of a low temperature
884 zircon outgrowth. *Contributions to Mineralogy and Petrology* (in press).
885 Heaney, P.J., Vicenzi, E.P., Giannuzzi, L.A. and Livi, K.J.T. (2001) Focused ion beam milling: A
886 method of site-specific sample extraction for microanalysis of Earth and planetary materials.
887 *American Mineralogist*, **86**, 1094–1099.
888 Heard, C.D.K., Papike, J.J. and Brearley, A.J. (2001) Oxygen fugacity of martian basalts from
889 electron microprobe oxygen and TEM-EELS analyses of Fe-Ti oxides. *American*
890 *Mineralogist* **86**, 1015–1024.
891 Heatherington, C. (2004) Aberration correction for TEM. *Materials Today*, December, 50-55.
892 Hochella, M.F.Jr., Moore, J.N., Golla, U. and Putnis, A. (1999) A TEM study of samples from
893 acid mine drainage systems: Metal-mineral association with implications for transport.
894 *Geochimica et Cosmochimica Acta*, **63**, 3395–3406.
895 Houben, L., Thust, A. and Urban, K. (2006) *Ultramicroscopy,* **106,** 200–214.
896 Jacob, D., Cordier, P., Morniroli, J.P. and Schertl, H.P. (2009) Application of precession electron
897 diffraction to the characterization of (021) twinning in pseudo-hexagonal coesite. *American*
898 *Mineralogist*, **94**, 684–692.
899 Janney, D.E. and Wenk, H-R (1999) Peristerite exsolution in metamorphic plagioclase from the
900 Lepontine Alps: An analytical and transmission electron microscope study. *American*
901 *Mineralogist*, **84**, 517–527.
902 Janney, D.E., Cowley, J.M. and Buseck, P.R. (2000) Structure of synthetic 2-line ferrihydrite by
903 electron nanodiffraction. *American Mineralogist*, **85**, 1180–1187.

904 Janney, D.E., Cowley, J.M. and Buseck, P.R. (2001) Structure of synthetic 6-line ferrihydrite by
905 electron nanodiffraction. *American Mineralogist*, **86**, 327–335.
906 Kirkland, A.I. and Meyer, R.R. (2004) “Indirect” high-resolution transmission electron
907 microscopy: Aberration measurement and wavefunction reconstruction. *Microscopy and*
908 *Microanalysis*, **10**, 401–413.
909 Kirkland, A., Chang, L-U., Haigh, S. and Hetherington, C. (2008) Transmission electron
910 microscopy without aberrations: Applications to materials science. *Current and Applied*
911 *Physics*, **8**, 425–428.
912 Lee, M.R. (1993) The petrography, mineralogy and origins of calcium sulphate within the Cold
913 Bokkeveld CM carbonaceous chondrite. *Meteoritics*, **28**, 53–62.
914 Lee, M.R. and Parsons, I. (2003) Microtextures of authigenic Or-rich feldspar in the Upper
915 Jurassic Humber Group, UK North Sea. *Sedimentology*, **50**, 597–608.
916 Lee, M.R. and Smith, C.L. (2006) Scanning transmission electron microscopy using a SEM:
917 applications to mineralogy and petrology. *Mineralogical Magazine*, **70**, 561-572.
918 Lee, M.R. and Ellen, R. (2008) Aragonite in the Murray (CM2) carbonaceous chondrite:
919 implications for parent body compaction and aqueous alteration. *Meteoritics and Planetary*
920 *Science*, **43**, 1219–1231.
921 Lee, M.R., Russell, S.S., Arden, J.W. and Pillinger, C.T. (1995) Nierite (Si_3N_4), a new mineral
922 from ordinary and enstatite chondrites. *Meteoritics*, **30**, 387–98.
923 Lee, M.R., Bland, P.A. and Graham, G. (2003) Preparation of TEM samples by focused ion beam
924 (FIB) techniques: applications to the study of clays and phyllosilicates in meteorites.
925 *Mineralogical Magazine*, **67**, 581–592.
926 Lee M.R., Brown D.J., Smith C.L., Hodson M.E., MacKenzie, M. and Hellmann R. (2007)
927 Characterisation of mineral surfaces using FIB and TEM: A case study of naturally-
928 weathered alkali feldspars. *American Mineralogist*, **92**, 1383−1394.
929 Lee, M.R., Hodson, M.E., Brown, D.J., MacKenzie, M. and Smith, C.L. (2008*a*) The composition
930 and crystallinity of the near-surface regions of weathered alkali feldspars. *Geochimica et*
931 *Cosmochimica Acta*, **72**, 4962–4975.
932 Lee, M.R., Brown, D. J., Hodson, M.E., MacKenzie, M. and Smith, C.L. (2008*b*) Weathering
933 microenvironments on feldspar surfaces: implications for understanding fluid-mineral
934 reactions in soils. *Mineralogical Magazine*, **72**, 1319–1328.
935 Lee, S., Kim, Y-M. and Kim, Y-J. (2007) Formation of crystalline silicon in kaolinite by electron
936 beam irradiation and in situ heating in the HVEM. *Journal of Electron Microscopy*, **56**, 153–
937 155.
938 Leppard, G.G. (2008) Nanoparticles in the environment as revealed by transmission electron
939 microscopy: Detection, characterisation and activities. *Current Nanoscience*, **4**, 278–301.
940 Leroux, H. (2001) Microstructural shock signatures of major minerals in meteorites. *European*
941 *Journal of Mineralogy*, **13**, 253-272.
942 Leroux, H., Rietmeijer, F.J.M., Velbel, M.A., Brearley, A.J., Jacob, D., Langenhorst, F., Bridges,
943 J.C., Zega T.J., Stroud, R.M., Cordier, P., Harvey, R.P., Lee, M., Gounelle, M. and

944 Zolensky, M.E. (2008). A TEM study of thermally modified comet 81P/Wild 2 dust particles
945 by interactions with the aerogel matrix during the Stardust capture process. *Meteoritics and*
946 *Planetary Science,* **43**, 1–24.
947 Lewis, R.S., Ming, T., Wacker, J.F., Anders, E. and Steel, E. (1987) Interstellar diamonds in
948 meteorites. *Nature*, **326**, 160–162.
949 Loomer, D.B., Al, T.A., Weaver, L. and Cogswell, S. (2007) Manganese valence imaging in Mn
950 minerals at the nanoscale using STEM-EELS. *American Mineralogist*, **92**, 72–79.
951 Loretto, M.H. (1994) *Electron beam analysis of materials*. 2nd edition, Chapman and Hall,
952 London, 272 pp.
953 Ma, C., Goreva, J.S. and Rossman, G.R. (2002) Fibrous nanoinclusions in massive rose quartz:
954 HRTEM and AEM investigations. *American Mineralogist*, **87**, 269–276.
955 McLaren, A.C. (1991) *Transmission electron microscopy of minerals and rocks*. Cambridge
956 University Press, 399 p.
957 Midgley, P.A. and Weyland, M. (2003) 3D electron microscopy in the physical sciences: the
958 development of Z-contrast and EFTEM tomography. *Ultramicroscopy*, **96**, 413–431.
959 Midgley, P.A. and Dunin-Borkowski, R.E. (2009) Electron tomography and holography in
960 materials science. *Nature Materials*, **8**, 271–280.
961 Mikouchi, T., Zolensky, M., Ivanova, M., Tachikawa, O., Komatsu, M., Le, L. and Gounelle, M.
962 (2009) Dmitryivanovite: A new high-pressure calcium aluminium oxide from the Northwest
963 Africa 470 CH3 chondrite characterized using electron backscatter diffraction analysis.
964 *American Mineralogist*, **94**, 746–750.
965 Moore, K.T., Elbert, D.C. and Veblen, D.R. (2001) Energy-filtered transmission electron
966 microscopy (EFTEM) of intergrown pyroxenes. *American Mineralogist*, **86**, 814–825.
967 Mugnaioli, E., Capitani, G., Nieto, F. and Mellini, M. (2009) Accurate and precise lattice
968 parameters by selected-area electron diffraction in the transmission electron microscope.
969 *American Mineralogist*, **94**, 793–800.
970 Muller, D.A. (2009) Structure and bonding at the atomic scale by scanning transmission electron
971 microscopy. *Nature Materials*, **8**, 263–270.
972 O'Keefe, M.A. (2008) Seeing atoms with aberration-corrected sub-Angstrom electron microscopy.
973 *Ultramicroscopy*, **108**, 196–209.
974 Obst, M., Gasser, P., Mavrocordatos, D. and Dittrich, M. (2005) TEM-specimen preparation of
975 cell/mineral interfaces by Focused Ion Beam milling. *American Mineralogist*, **90**, 1270–
976 1277.
977 Palenik, C.S., Utsunomiya, S., Reich, M., Kesler, S.E., Wang, L. and Ewing, R.C. (2004)
978 "Invisible" gold revealed: Direct imaging of gold nanoparticles in a Carlin-type deposit.
979 *American Mineralogist,* **89**, 1359–1366.
980 Peacor, D.R. (1992*a*) Diagenesis and low grade metamorphism of shales and slates. Pp 335–380
981 in: *Minerals and reactions at the atomic scale: Transmission electron microscopy* (P.R.
982 Buseck, editor). Reviews in Mineralogy **27**, Mineralogical Society of America.

983 Peacor, D.R. (1992*b*) Analytical electron microscopy: X-ray analysis. Pp 113–140 in: *Minerals*
984 *and reactions at the atomic scale: Transmission electron microscopy* (P.R. Buseck, editor).
985 Reviews in Mineralogy **27**, Mineralogical Society of America.
986 Prior, D.J., Boyle, A.P., Brenker, F., Cheadle, M.C., Day, A., Lopez, G., Peruzzo, L., Potts, G.J.,
987 Reddy, S., Spiess, R., Timms, N.E., Trimby, P., Wheeler, J. and Zetterstrom, L. (1999) The
988 application of electron backscatter diffraction and orientation contrast imaging in the SEM to
989 textural problems in rocks. *American Mineralogist*, **84**, 1741–1759.
990 Putnis, A. (1992) Introduction to Mineral Sciences. Cambridge University Press, 457 pp.
991 Reeder, R.J. (1992) Carbonates: Growth and alteration microstructures. Pp 381–424 in: *Minerals*
992 *and reactions at the atomic scale: Transmission electron microscopy* (P.R. Buseck, editor).
993 Reviews in Mineralogy **27**, Mineralogical Society of America.
994 Reddy, S.M., Timms, N.E., Trimby, P., Kinny, P.D., Buchan, C. and Blake, K. (2006) Crystal-
995 plastic deformation of zircon: A defect in the assumption of chemical robustness. *Geology*,
996 **34,** 257-260**.**
997 Seydoux-Guillaume, A.M., Goncalves, P., Wirth, R. and Deutsch, A. (2003) Transmission
998 electron microscope study of polyphase and discordant monazites: Site-specific specimen
999 preparation using the focused ion beam technique. *Geology*, **31,** 973–976**.**
1000 Self, P. (1992) High-Resolution Image Simulation and Analysis. Pp 85–112 in: *Minerals and*
1001 *reactions at the atomic scale: Transmission electron microscopy* (P.R. Buseck, editor).
1002 Reviews in Mineralogy **27**, Mineralogical Society of America.
1003 Smith, D.J. (2008) Ultimate resolution in the electron microscope? *Materials Today*, 30–38.
1004 Steeds, J.W. and Mornirolin, J.-P. (1992) Selected Area Electron Diffraction (SAED) and
1005 Convergent Beam Electron Diffraction (CBED). Pp 37–84 in: *Minerals and reactions at the*
1006 *atomic scale: Transmission electron microscopy* (P.R. Buseck, editor). Reviews in
1007 Mineralogy **27**, Mineralogical Society of America.
1008 Stephan, T., Jessberger, E.K., Klöck, W., Rulle, H. and Zehnpfenning, J. (1994) TOF-SIMS
1009 analysis of interplanetary dust. *Earth and Planetary Science Letters,* **128**, 453–467.
1010 Stroud, R.M., Alexander, C.M.O'D. and MacPherson, G.J. (2000) A precise new method of
1011 microsampling chondritic material for transmission electron microscope analysis:
1012 preliminary application to calcium-aluminium-rich inclusions and associated matrix material
1013 in the Vigarano CV3 meteorite. *Meteoritics and Planetary Sciences Supplement*, **35**, A153–
1014 154.
1015 Urban, K.W. (2008) Studying atomic structures by aberration-corrected transmission electron
1016 microscopy. *Science*, **321**, 506–510.
1017 Urban, K.W. (2009) Is science prepared for atomic resolution electron microscopy? *Nature*
1018 *Materials*, **8**, 260–262.
1019 Utsunomiya, S. and Ewing, R.C. (2003) Application of high-angle annular dark field scanning
1020 transmission electron microscopy, scanning transmission electron microscopy-energy
1021 dispersive X-ray spectrometry, and energy-filtered transmission electron microscopy to the

1022 characterisation of nanoparticles in the environment. *Environmental Science and*
1023 *Technology*, **37**, 786–791.
1024 Utsunomiya, S., Palenik, C.S., Valley, J. W., Cavosie, A.J., Wilde, S.A. and Ewing, R. C. (2004)
1025 Nanoscale occurrence of Pb in an Archaen zircon. *Geochimica et Cosmochimica Acta*, **68**,
1026 4679–4686.
1027 Utsunomiya, S., Valley, J.W., Cavosie, A.J., Wilde, S.A. and Ewing, R.C. (2007) radiation
1028 damage and alteration of zircon from a 3.3 Ga porphyritic granite from the Jack Hills,
1029 Western Australia. *Chemical Geology,* **236**, 91–111.
1030 Utsunomiya, S., Kersting, A.B. and Ewing, R.C. (2009) Groundwater nanoparticles in the far-field
1031 of the Nevada test site: Mechanism for radionuclide transport. *Environmental Science and*
1032 *Technology*, **43**, 1293–1298.
1033 Van Ngo, V., Hernandez, M. and Roth, B. (2007) STEM imaging of lattice fringes and beyond in a
1034 UHR in-lens field-emission SEM. *Microscopy Today*, 12–16.
1035 Watt, L.E., Bland, P.A., Prior, D.J. and Russell, S.S. (2006) Fabric analysis of Allende matrix
1036 using EBSD. *Meteoritics and Planetary Science*, **41**, 989–1001.
1037 Williams, D.B. and Carter, C.B. (1996) *Transmission Electron Microscopy—A Textbook for*
1038 *Materials Science*. Plenum Press, New York and London, 729 pp.
1039 Wirth, R. (2004) Focused Ion Beam (FIB): A novel technology for advanced application of micro-
1040 and nanoanalysis in geosciences and applied mineralogy. *European Journal of Mineralogy*,
1041 **16**, 863–876.
1042 Wirth, R. (2009) Focused ion beam combined with SEM and TEM: Advanced analytical tools for
1043 studies of chemical composition, microstructure and crystal structure in geomaterials on a
1044 nanometer scale. *Chemical Geology*, **261**, 217–229.
1045 Xin, H.J., Intaraprasonk, V. and Muller, D.A. (2008) Depth sectioning of individual dopant atoms
1046 with aberration-corrected scanning transmission electron microscopy. *Applied Physics*
1047 *Letters*, **92**, 013125.
1048 Zega, T.J., Garvie, L.A.J. and Buseck, P.R. (2003) Nanometer-scale measurements of iron
1049 oxidation states of cronstedtite from primitive meteorites. *American Mineralogist*, **88**, 1169–
1050 1172.
1051 Zega, T.J., Nittler, L.R., Busemann, H., Hoppe, P. and Stroud, R.M. (2007) Coordinated isotopic
1052 and mineralogical analyses of planetary materials enabled by in situ lift-out with a focused
1053 ion beam scanning electron microscope. *Meteoritics and Planetary Science,* **42**, 1373–1386.
1054 Zhang, S. and Veblen, D.R. (2007) Chemical and structural variations at augite (100) deformation
1055 twin boundaries. *American Mineralogist*, **92**, 1833–1837.
1056 Zhu, C., Veblen, D.R., Blum, A.E. and Chipera, S.J. (2006) Naturally weathered feldspar surfaces
1057 in the Navajo Sandstone aquifer, Black Mesa, Arizona: Electron microscopic
1058 characterization. *Geochimica et Cosmochimica Acta*, **65**, 3459–3474.
1059 Ziegler, J.F. (2003) The stopping and range of ions in matter (SRIM-2003). Annapolis, Maryland.
1060 http://www.srim.org

1061 Zolensky, M., Nakamura-Messenger, K., Fletcher, L. and See, T. (2008) Curation, spacecraft
1062 recovery, and preliminary examination for the Stardust mission: A perspective from the
1063 curational facility. *Meteoritics and Planetary Science,* **43**, 5–21.
1064
1065

1066
1067 FIG. 1. Bright-field TEM images of acid-resistant residues of primitive meteorites. (*a*) A residue
1068 containing grains of a wide range of shapes and sizes dispersed over a carbon film (grey). The film
1069 has micrometre-sized holes (white) and is supported by a copper grid (black). (*b*) An acid-resistant
1070 residue of the Indarch meteorite (EH4 enstatite chondrite). A crystal of nierite (Si_3N_4), which is
1071 oriented with its [11-20] zone axis parallel to the incident electron beam, rests on the holey carbon
1072 film and is surrounded by nanometre sized diamonds. The corresponding SAED pattern (inset)
1073 contains spots from the nierite and rings from the nanodiamonds. The innermost ring has a d-
1074 spacing of 0.206 nm, corresponding to diamond {111} planes.
1075
1076 FIG. 2. Dark-field STEM image of cometary grains embedded in silica aerogel (uppermost image)
1077 with corresponding Si, Mg, Fe and Ca X-ray maps acquired from the boxed area. The grains were
1078 collected during the NASA Stardust mission. The Mg-rich fragments (numbered 1 to 6) may be
1079 the remains of two silicate grains that shattered during cutting by ultramicrotome, with one of
1080 these grains also being rich in calcium (fragments 1–3). The small Fe-rich grains are Fe-sulphides.
1081 Reproduced from Leroux et al. (2008) with permission from *Meteoritics & Planetary Science,* ©
1082 2008 by the Meteoritical Society.
1083
1084 FIG. 3. Images of FIB-produced foils. (*a*) Secondary electron SEM image of a foil cut from the
1085 surface of a weathered alkali feldspar grain. False colouring highlights a fungal hypha (yellow),
1086 the foil (pink) and its platinum strap (green). (*b*) Secondary electron SEM image of a foil that has
1087 been cut from weathering products encrusting the surface of a soil alkali feldspar. The foil was
1088 milled to electron transparency *in-situ* using a single-beam FIB and fell away after its sides and
1089 base had been cut free. (*c*) Dark-field low-voltage scanning transmission electron microscope
1090 image of a foil that has been placed onto a holey carbon film using an *ex-situ* micromanipulator.
1091 (*d*) Secondary electron SEM image showing three foils (arrowed) that have been lifted out *in-situ*
1092 and welded to the tines of a holder using a dual-beam FIB instrument.
1093
1094 FIG. 4. Diagram showing the relative positions of the main components of a microscope that can
1095 operate both in TEM and STEM modes. Those components used for both TEM and STEM work
1096 are named in black whereas components used in TEM only are in blue and in STEM only are in
1097 red. Note that dedicated STEM instruments may differ significantly in their configuration.
1098
1099 FIG. 5. Summary of the main signals used for (S)TEM imaging, electron diffraction and X-ray and
1100 electron spectroscopy. Modified from Williams and Carter (1996).
1101
1102 FIG. 6. Illustration of the collection semi-angles used by the different STEM electron detectors.
1103 Note that the bright-field (BF) detector may be integrated into the EELS system.
1104
1105 FIG. 7. (*a*) Bright-field STEM and (*b*) HAADF STEM image of a FIB-produced foil of the Acfer
1106 094 meteorite (Bland *et al.,* 2009). The sample contains high Z Fe-rich grains (Fe) in a lower Z
1107 silicate groundmass. The images were obtained after acquisition of an EDX spectrum map that
1108 used a ~1 nm spot at a 10 nm spacing; the dwell time was ~1 sec/point. A matrix of holes 'drilled'
1109 as a consequence of beam damage during analysis are clearly visible. (*c*) High-resolution HAADF
1110 STEM image of an Archaean zircon with an inset diffractogram. The small white spots are
1111 columns of atoms and lead is concentrated in the central brighter area of the image. Reprinted
1112 from Geochimica et Cosmochimica Acta, Vol. 68 (22), Utsunomiya, S., Palenik, C.S., Valley, J.

1113 W., Cavosie, A.J., Wilde, S.A. and Ewing, R.C., Nanoscale occurrence of Pb in an Archaen
1114 zircon, 4679-4686. Copyright (2004), with permission from Elsevier.
1115
1116 FIG. 8. Bright-field TEM images. (*a*) An alkali feldspar from the Klokken syenite intrusion
1117 containing a very fine-scale intergrowth of Albite-twinned albite (Aa), Pericline-twinned albite
1118 (Pa) and microcline (M). The foil is oriented with the incident beam parallel to the [001] zone axis
1119 of the Pericline-twinned albite. (*b*) A detrital alkali feldspar grain from an oil reservoir in the UK
1120 North Sea; the interface between the grain and its K-feldspar overgrowth runs from the NE to SW
1121 corner of the image. In the lower right is microcline of the detrital grain that contains three small
1122 albite exsolution lamellae. Albite and Pericline twins in the microcline are highlighted by bend
1123 contours (B) in the foil. The overgrowth is in the upper left and its mottled appearance is due to a
1124 subgrain microtexture and an abundance of dislocations on subgrain boundaries.
1125
1126 FIG. 9. High resolution TEM image of amphibole from a weathered gedrite gneiss that has been
1127 partially and isovolumetrically transformed to smectite, which fills a SE-NW oriented channel.
1128 Islands of amphibole remain between the smectite and the arrows indicate the smectite reaction
1129 front. Reprinted from Geochimica et Cosmochimica Acta, Vol. 58 (5), Banfield, J.F and Barker,
1130 W.W., Direct observation of reactant-product interfaces formed in natural weathering of exsolved,
1131 defective amphibole to smectite: Evidence for episodic, isovolumetric reactions involving
1132 structural inheritance, 1419-1429. Copyright (1994), with permission from Elsevier.
1133
1134 FIG. 10. High-resolution TEM images of dumortierite-related crystals in an acid-resistant residue
1135 of rose quartz. The images show single fibres viewed down the (*a*) [112] and (*b*) [110] directions.
1136 These images are matched with computer simulations of the crystal structure (inset). A
1137 corresponding SAED pattern is also inset to (*a*). From Ma, C., Goreva, J.S. and Rossman, G.R.
1138 (2002) Fibrous nanoinclusions in massive rose quartz: HRTEM and AEM investigations.
1139 American Mineralogist, 87, 269–276. Reproduced with permission from the Mineralogical Society
1140 of America.
1141
1142 FIG. 11. Electron nanodiffraction (END) patterns of kaolinite. (*a*) Pattern acquired with the
1143 electron beam oriented parallel to 0.72 nm silicate layers. (*b*) Pattern acquired with the electron
1144 beam perpendicular to the layers. (*c*) Pattern showing the effects of radiation damage resulting
1145 from less than 1 second of electron irradiation. Reprinted from Micron, 35 (5), Cowley, J.M.,
1146 Applications of electron nanodiffraction, 345-360, Copyright (2004), with permission from
1147 Elsevier.
1148
1149 FIG. 12. Illustrations of the various mechanisms by which a mineral can be damaged during
1150 (S)TEM work.
1151
1152 FIG. 13. Parts of EELS spectra of γ-Mg_2SiO_4. In [a] the weak Si $L_{2,3}$ edge is just visible on the
1153 strongly sloping background. [b] is a background-subtracted single spectrum acquired for 2
1154 seconds. [c] has been made from 15 gain-shifted and background-subtracted spectra. The
1155 intensities of [b] and [c] are ten times that of [a]. Reproduced from Garvie, L.A.J. and Buseck,
1156 P.R. (1999) Bonding in silicates: Investigation of the Si $L_{2,3}$ edge by parallel electron energy-loss
1157 spectroscopy. *American Mineralogist*, **84**, 946–964. With permission from the Mineralogical
1158 Society of America.

1159

1160 FIG. 14. EELS spectra showing $L_{2,3}$ edges of elemental Fe and minerals containing single valent
1161 Fe. Reprinted by permission from Macmillan Publishers Ltd: Garvie, L.A.J. and Buseck, P.R.
1162 (1998) Ratios of ferrous to ferric iron from nanometre-sized areas in minerals. Nature 396, 667-
1163 670, copyright (1998).

1164

1165 FIG. 15. EFTEM image of desert varnish from the Sonoran Desert, southwestern Arizona (Garvie
1166 *et al.,* 2008). The image is a composite of 20 separate iron (purple) and manganese (green)
1167 EFTEM images acquired from a FIB-produced foil. Most of the black areas of the image are
1168 silica-rich regions.

1169

1170 FIG. 16. Bright-field (*a*) and dark-field (*b*) LV-STEM images of kaolinite crystals supported on a
1171 carbon film. (*c*) Bright-field TEM (upper half) and corresponding dark-field LV-STEM image
1172 (lower half) of a foil cut from the matrix of the Murchison (CM2 carbonaceous chondrite)
1173 meteorite using the FIB technique. The two images are complementary and show that the darker
1174 grains in the bright-field TEM (Fe-rich phyllosilicates, metal and sulphides) correspond to higher
1175 Z grains (light grey) in dark-field LV-STEM. These high-Z grains are enclosed by lower Z Mg-
1176 rich phyllosilicates. (*d*) Dark-field LV-STEM image of the Murchison foil showing Fe-rich
1177 phyllosilicates (Fe-ph) enclosed by very finely crystalline Mg-rich phyllosilicates (Mg-ph)
1178 containing readily resolvable crystals a few tens of nanometres in size.

1179

(a)

50 μm

(b)

Hole

Nierite

Diamond

500 nm

Compressed
aerogel
1 μm

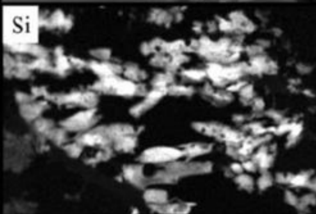
Si

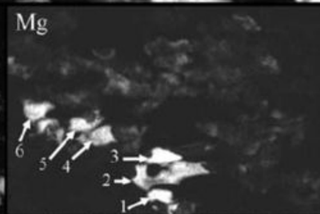
Mg
6
5
4
3
2
1

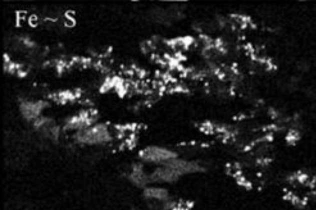
Fe ~ S

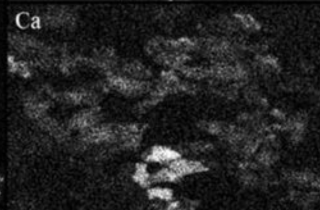
Ca

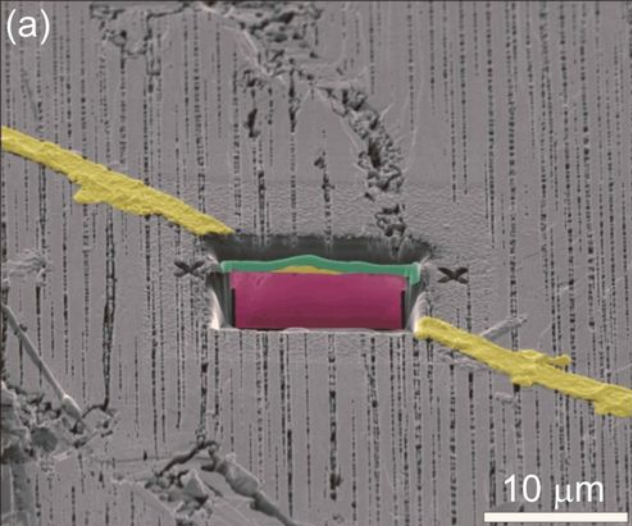
(a)
10 μm
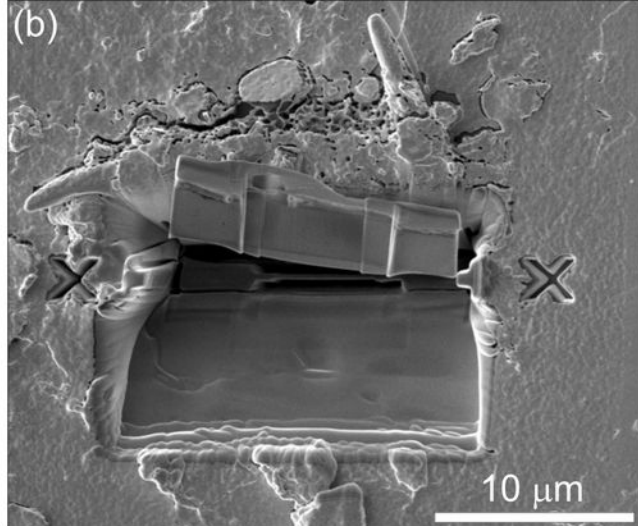
(b)
10 μm
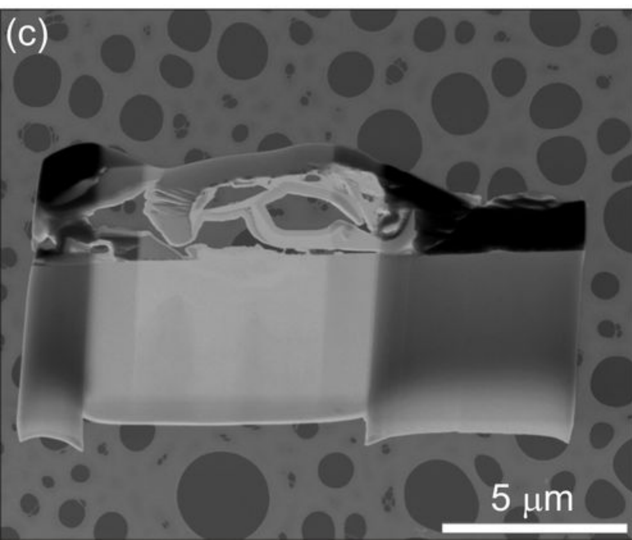
(c)
5 μm
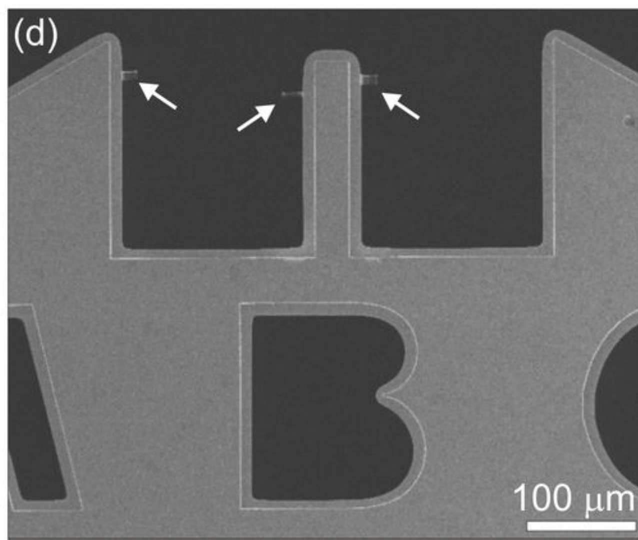
(d)
100 μm

W/Lab$_6$ thermionic gun
or field-emission tip
Optic axis

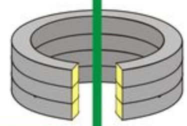
C1 & C2 (condenser)
lenses

Condenser aperture strip

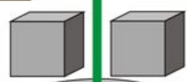
Scan coils

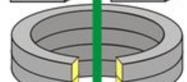
C3 (condenser) lens

X-ray
detector

Thin sample

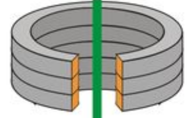
Objective
lens

Objective aperture strip

Selected area aperture strip

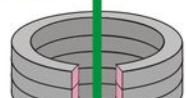
Intermediate
lens

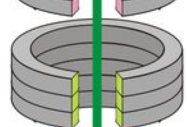
Projector
lens

Electron
detectors

Image capture

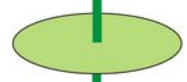
Fluorescent screen (retractable)

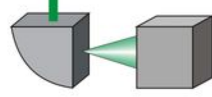
Magnetic prism &
EELS spectrometer

Image capture

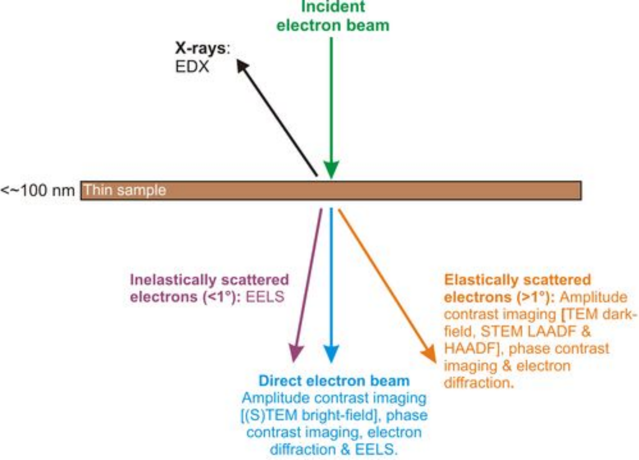
Incident
electron beam
X-rays:
EDX
<~100 nm
Thin sample
Inelastically scattered
electrons (<1°): EELS
Elastically scattered
electrons (>1°): Amplitude
contrast imaging [TEM dark-
field, STEM LAADF &
HAADF], phase contrast
imaging & electron
diffraction.
Direct electron beam
Amplitude contrast imaging
[(S)TEM bright-field], phase
contrast imaging, electron
diffraction & EELS.

Scanning
incident beam

Thin sample

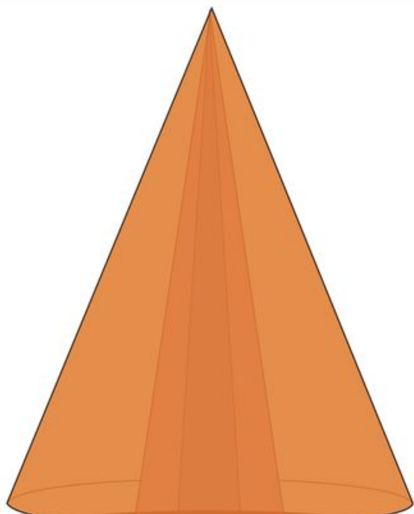

HAADF ~3-10°
LAADF ~0.5-3°

BF <~0.5°

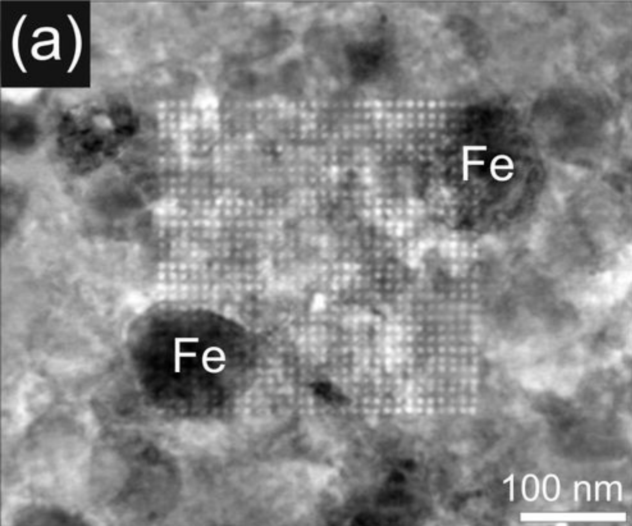

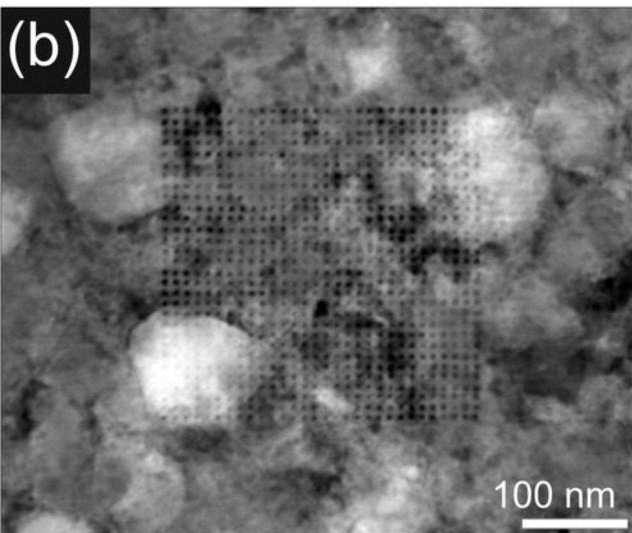

(c)
a
c
5 nm

(a)
M
Aa
Pa
100 nm
(b)
B
B
500 nm

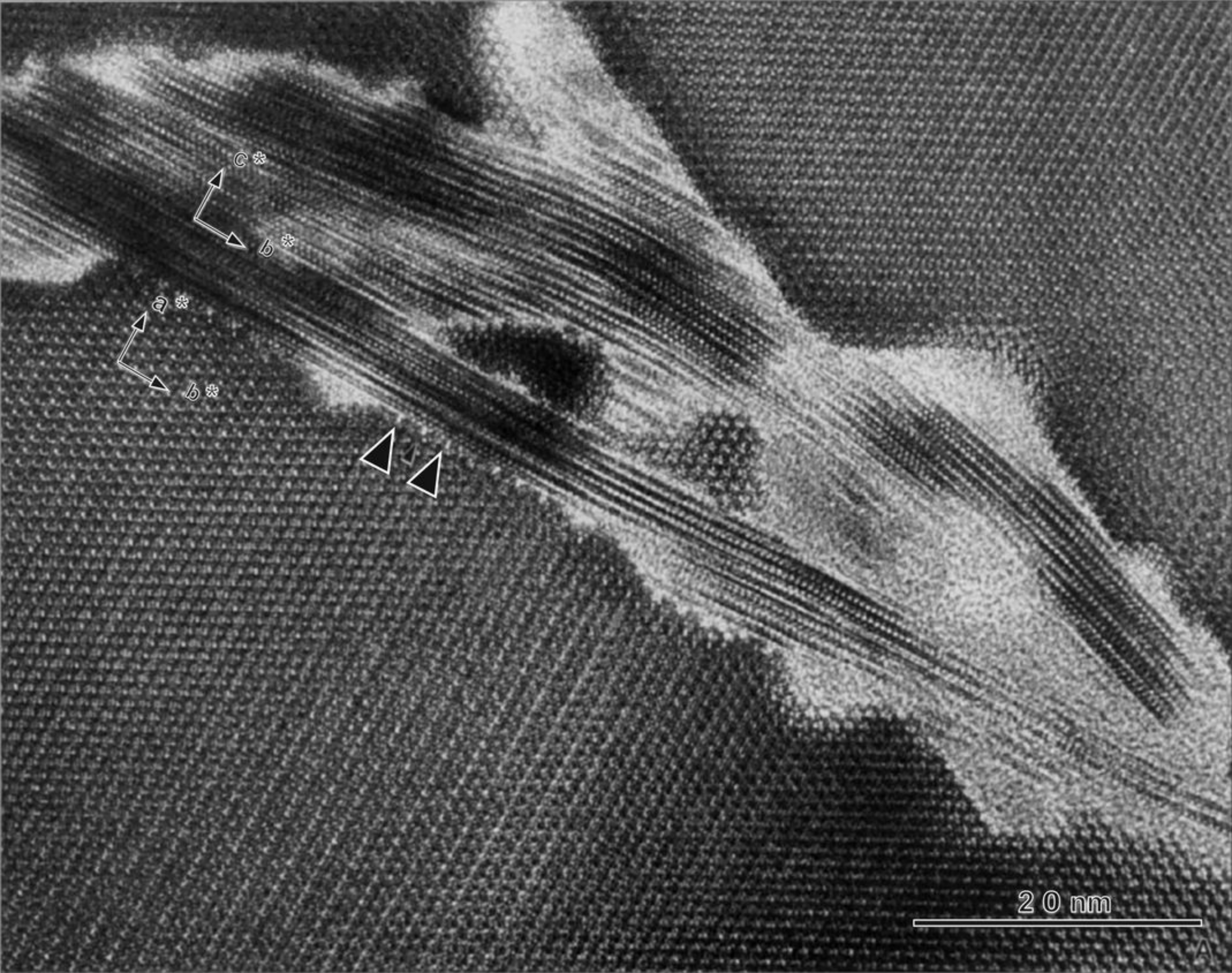
c*
b*
a*
b*
2 0 nm
A

(a)

2 nm

[02-1]*

[1-10]*

$02\bar{1}$

$\bar{2}20$

Simulation

(b)

2 nm

c

[1-10]*

Simulation

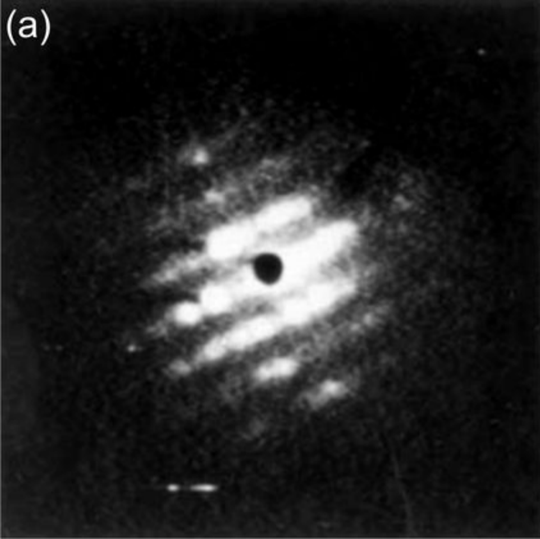
(a)
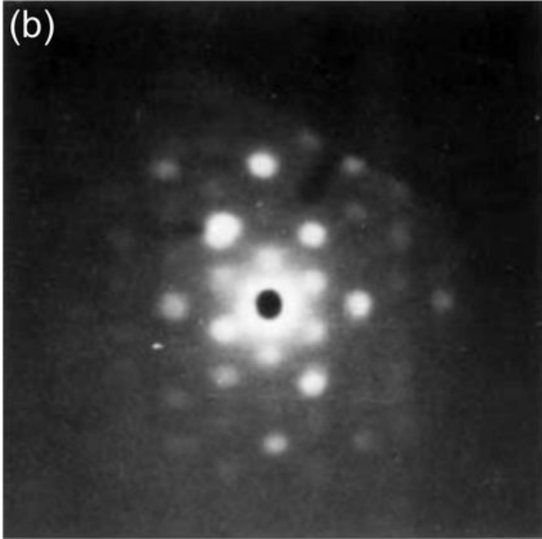
(b)
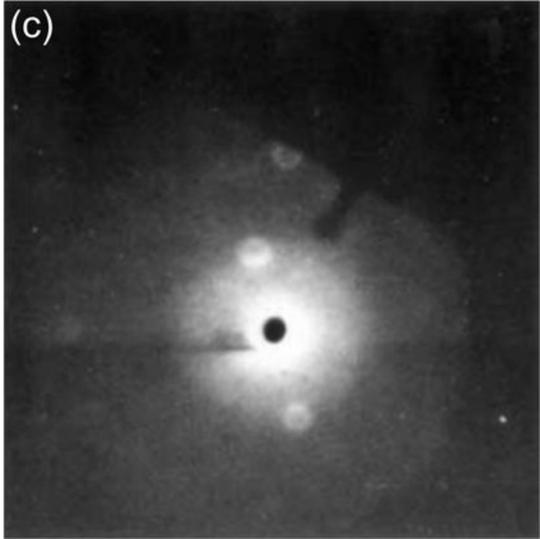
(c)

Structural water
High Z element
Low Z element
Bond
Incident beam
Sputtering
C Carbon

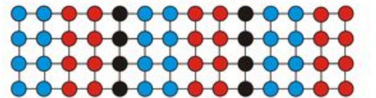

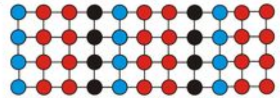

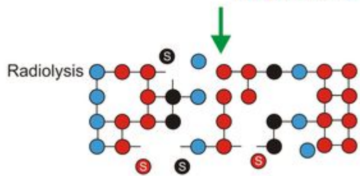

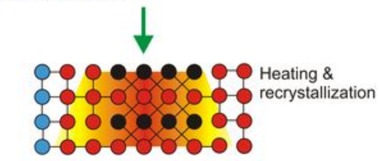

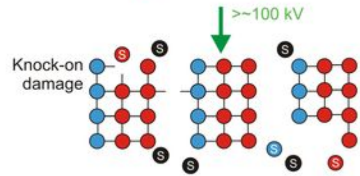

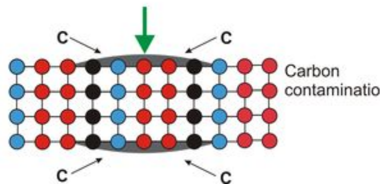

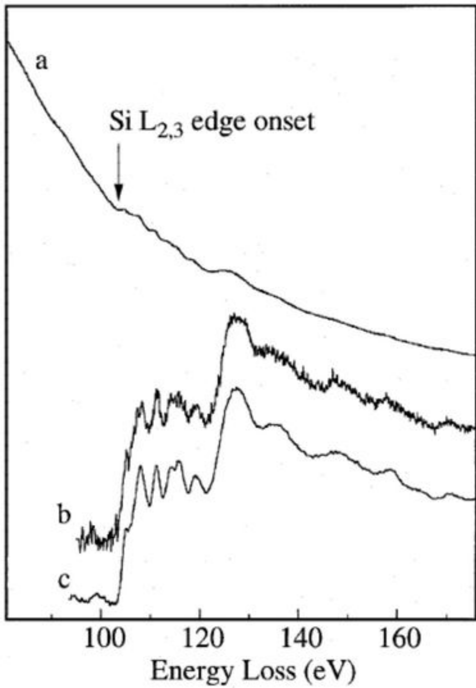
a
Si $L_{2,3}$ edge onset
b
c
100
120
140
160
Energy Loss (eV)

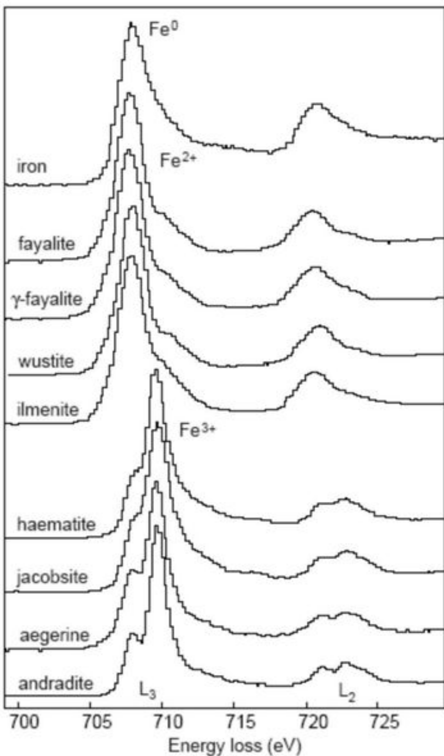

Fe0
Fe2+
Fe3+
iron
fayalite
γ-fayalite
wustite
ilmenite
haematite
jacobsite
aegerine
andradite
L3
L2
700
705
710
715
720
725
Energy loss (eV)

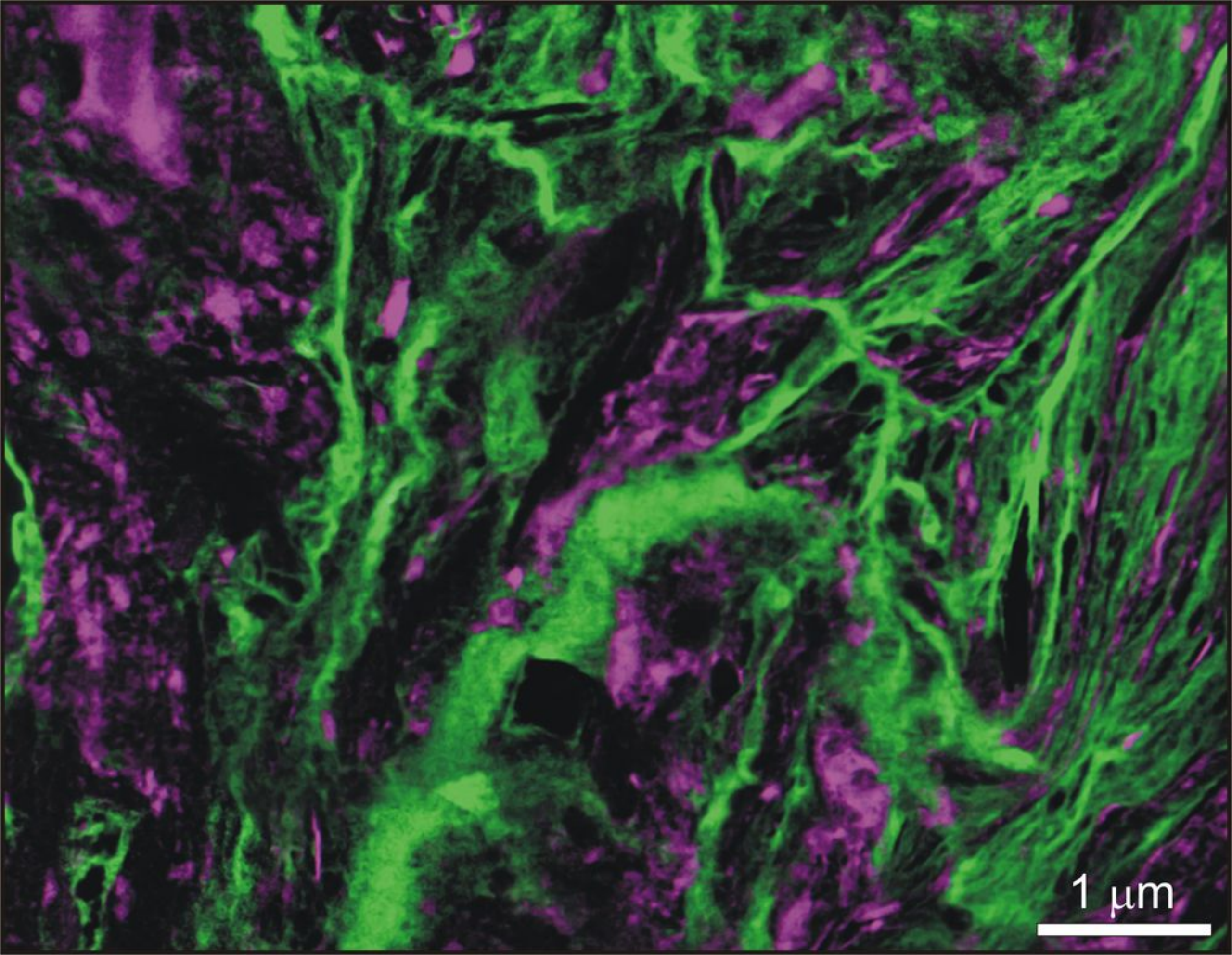
1 μm

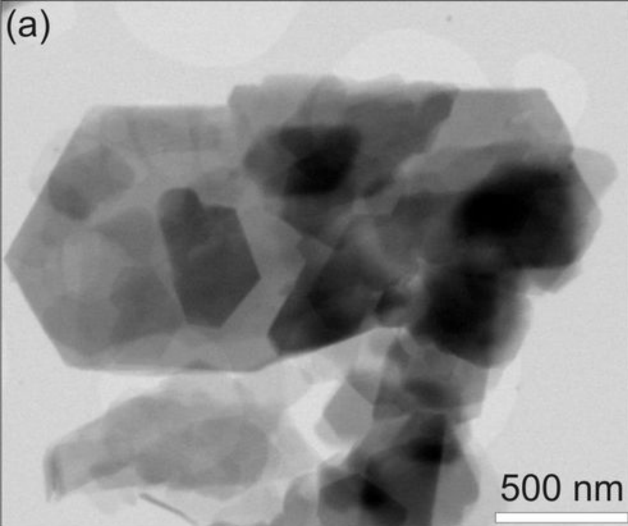
(a)
500 nm
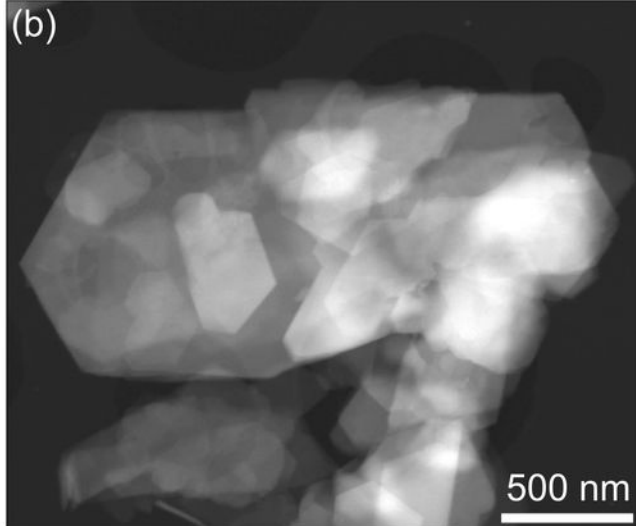
(b)
500 nm
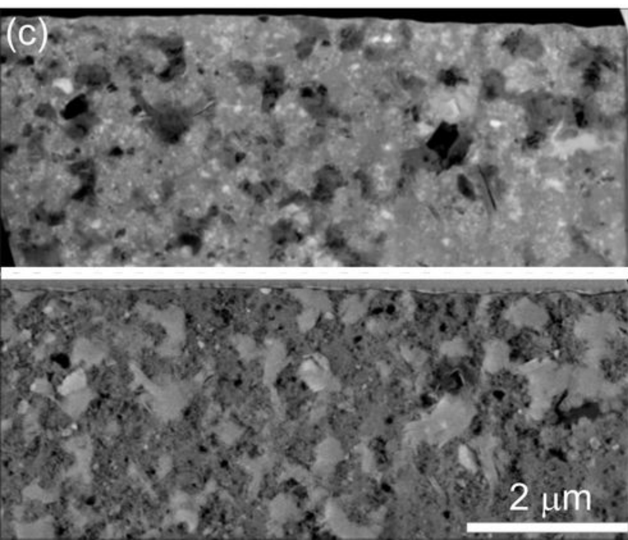
(c)
2 μm
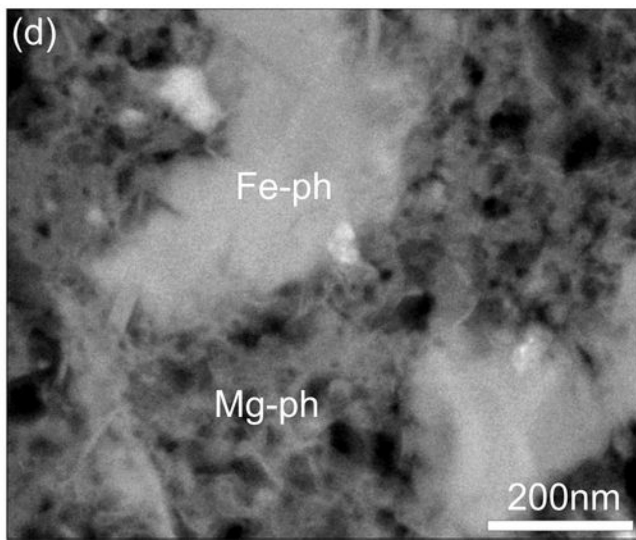
(d)
Fe-ph
Mg-ph
200nm